OPEN ACCESS
CellPress

Cell Reports
Article

Dysregulated Expression of Neuregulin-1 by Cortical Pyramidal Neurons Disrupts Synaptic Plasticity

Amit Agarwal,[1,7,8] Mingyue Zhang,[2,8] Irina Trembak-Duff,[2,8] Tilmann Unterbarnscheidt,[1,8] Konstantin Radyushkin,[3,9] Payam Dibaj,[1] Daniel Martins de Souza,[4,10] Susann Boretius,[5] Magdalena M. Brzózka,[1,11] Heinz Steffens,[6] Sebastian Berning,[6] Zenghui Teng,[2] Maike N. Gummert,[1] Martesa Tantra,[3] Peter C. Guest,[4] Katrin I. Willig,[6] Jens Frahm,[5] Stefan W. Hell,[6] Sabine Bahn,[4] Moritz J. Rossner,[1,11] Klaus-Armin Nave,[1] Hannelore Ehrenreich,[3] Weiqi Zhang,[2,*] and Markus H. Schwab[1,12,*]

[1]Department of Neurogenetics, Max Planck Institute of Experimental Medicine, 37075 Göttingen, Germany
[2]Laboratory of Molecular Psychiatry, Department of Psychiatry, University of Münster, 48149 Muenster Germany
[3]Clinical Neuroscience, Max Planck Institute of Experimental Medicine, 37075 Göttingen, Germany
[4]Institute of Biotechnology, University of Cambridge, Cambridge CB2 1QT, UK
[5]Biomedizinische NMR Forschungs GmbH, Max Planck Institute of Biophysical Chemistry, 37077 Göttingen, Germany
[6]Department of NanoBiophotonics, Max Planck Institute for Biophysical Chemistry, 37077 Göttingen, Germany
[7]Solomon H. Snyder Department of Neuroscience, Johns Hopkins University, Baltimore, MD 21025, USA
[8]Co-first author
[9]Present address: Department of Physiological Chemistry, Focus Program Translational Neurosciences, Johannes Gutenberg University of Mainz, 55131 Mainz, Germany
[10]Present address: Laboratory of Neuroproteomics, Department of Biochemistry, Institute of Biology, State University of Campinas (UNICAMP), Campinas, Sao Paulo 13083-970, Brazil
[11]Present address: Department of Psychiatry, Ludwig-Maximilian-University Munich, 81377 Munich, Germany
[12]Present address: Cellular Neurophysiology, Hannover Medical School, 30625 Hannover, Germany
*Correspondence: wzhang@uni-muenster.de (W.Z.), schwab@em.mpg.de (M.H.S.)
http://dx.doi.org/10.1016/j.celrep.2014.07.026

SUMMARY

Neuregulin-1 (*NRG1*) gene variants are associated with increased genetic risk for schizophrenia. It is unclear whether risk haplotypes cause elevated or decreased expression of NRG1 in the brains of schizophrenia patients, given that both findings have been reported from autopsy studies. To study NRG1 functions in vivo, we generated mouse mutants with reduced and elevated NRG1 levels and analyzed the impact on cortical functions. Loss of NRG1 from cortical projection neurons resulted in increased inhibitory neurotransmission, reduced synaptic plasticity, and hypoactivity. Neuronal overexpression of cysteine-rich domain (CRD)-NRG1, the major brain isoform, caused unbalanced excitatory-inhibitory neurotransmission, reduced synaptic plasticity, abnormal spine growth, altered steady-state levels of synaptic plasticity-related proteins, and impaired sensorimotor gating. We conclude that an "optimal" level of NRG1 signaling balances excitatory and inhibitory neurotransmission in the cortex. Our data provide a potential pathomechanism for impaired synaptic plasticity and suggest that human NRG1 risk haplotypes exert a gain-of-function effect.

INTRODUCTION

Neuregulin-1 (NRG1) is a pleiotropic growth and differentiation factor, which signals to receptor tyrosine kinases of the ErbB family (Falls, 2003). The human *NRG1* gene is a major schizophrenia susceptibility gene (Ayalew et al., 2012; Li et al., 2006), but the underlying link to pathophysiology is not known. Virtually all "at-risk" haplotypes map to noncoding regions of the human *NRG1* gene (Stefansson et al., 2002; Weickert et al., 2012), suggesting that altered NRG1 expression increases disease susceptibility. Indeed, both reduced and increased expression of distinct NRG1 variants have been observed in studies of postmortem brain tissue from schizophrenia patients (Bertram et al., 2007; Law et al., 2006). This includes elevated expression of membrane-bound "cysteine-rich domain" (CRD)-NRG1 (Weickert et al., 2012), the predominant NRG1 isoform in the human brain (Liu et al., 2011). CRD-NRG1 serves as a key regulator of myelination in the peripheral nervous system (Nave and Salzer, 2006) but is not required for myelin assembly in the CNS (Brinkmann et al., 2008), suggesting that it has distinct functions in the brain.

Heterozygous disruption of CRD-NRG1 in mice results in deficits in glutamatergic and cholinergic neurotransmission from the hippocampus to the amygdala (Jiang et al., 2013; Zhong et al., 2008) and impaired short-term memory (Chen et al., 2008). Genetic inactivation of ErbB4, the predominant neuronal NRG1 receptor in the brain, results in increased long-term potentiation (LTP) (Pitcher et al., 2008) and blocked NRG1-mediated LTP

suppression in hippocampal slice culture (Chen et al., 2010). In addition, loss of ErbB4 in mice leads to impaired interneuron development, reduced GABAergic neurotransmission (Del Pino et al., 2013; Fazzari et al., 2010; Neddens and Buonanno, 2010), and enhanced limbic epileptogenesis (Li et al., 2012; Tan et al., 2012), demonstrating an important role of ErbB4 signaling in the regulation of inhibitory cortical circuitry. In ''gain-of-function'' approaches, the treatment of cultured neurons or brain slices with the soluble epidermal-growth-factor-like domain of NRG1 was shown to induce transcription of mRNAs encoding neurotransmitter receptors (Ozaki et al., 1997); to modulate glutamatergic, GABAergic, cholinergic, and dopaminergic neurotransmission (Gu et al., 2005; Kwon et al., 2005; Ting et al., 2011; Woo et al., 2007); to suppress hippocampal synaptic plasticity (Huang et al., 2000; Kwon et al., 2005; Pitcher et al., 2011); and to promote dendritic spine growth (Cahill et al., 2013). Recently, transgenic mice with forebrain-specific overexpression of ''soluble'' immunoglobulin (Ig)-domain-containing NRG1 (''Ig-NRG1'') have been reported to display synaptic dysfunction and behavioral deficits (Yin et al., 2013a). Collectively, these studies suggest that NRG1 functions as a pleiotropic factor in the establishment and fine-tuning of cortical circuitry. In addition, these data support the hypothesis that both reduced and increased NRG1 signaling may interfere with synaptic efficacy. However, the effect of elevated CRD-NRG1 signaling has not been studied in vivo, and due to embryonic lethality of the *Nrg1*-null mutation (Meyer and Birchmeier, 1995), the consequences of a permanent loss of NRG1 on synaptic functions have not been elucidated.

Here, we have modeled the loss of all NRG1 isoforms and elevated CRD-NRG1 expression in conditional mouse mutants and transgenic mice. Our data provide potential pathomechanisms for cortical disconnectivity in response to chronically altered CRD-NRG1 signaling.

RESULTS

Hypoactivity and Impaired Fear-Conditioned Learning in the Absence of NRG1

Postnatal recombination of a conditional (''floxed'') *Nrg1* allele (Li et al., 2002) in forebrain projection neurons using a *CamKII-Cre* driver line (Minichiello et al., 1999) resulted in a 30%–75% reduction of NRG1 protein levels in homozygous floxed *Nrg1* mutants harboring the *CamKII-Cre* transgene (referred to as *CK*Nrg1*$^{f/f}$), depending on the cortical region analyzed (Figures 1A, S1A, and S1B). Even at 18 months of age, we observed no signs of neurodegeneration and inflammation in the hippocampus (Figure 1B) or white matter (Figure S1C) and no change in the levels of PSD95, ErbB4, and several glutamate receptor subunits in *CK*Nrg1*$^{f/f}$ mutants (Figures 1C, 1D, and S1D).

Next, we performed a behavioral analysis of *CK*Nrg1*$^{f/f}$ mutants. We found no significant effects on the startle response and prepulse inhibition (PPI) in *CK*Nrg1*$^{f/f}$ mutants (Figures S1E and S1F; data not shown). However, *CK*Nrg1*$^{f/f}$ mutants displayed hypoactivity in the open-field test at 3 months of age (Figure 1E). Hypoactivity in *CK*Nrg1*$^{f/f}$ mutants was not associated with increased general anxiety in the open-field test (Figure S1G). Administration of the noncompetitive NMDA receptor antagonist MK-801 induces hyperactivity and serves as a pharmacological model of psychosis (Deutsch et al., 1997). A single dose of MK-801 (0.3 mg/kg) administered to control mice (*Nrg1*$^{f/+}$) at 3 months (Figure 1F) and 12 months of age (Figure 1H) increased motor activity for more than 1 hr. In contrast, *CK*Nrg1*$^{f/f}$ mutants at 3 to 4 months of age showed a strong tendency for reduced MK-801-induced hyperactivity (Figure 1F). At 12 months of age, *CK*Nrg1*$^{f/f}$ mutants were no longer hypoactive in the open-field test (Figure 1G). However, MK-801-induced hyperactivity was significantly reduced in *CK*Nrg1*$^{f/f}$ mutants and rapidly declined to baseline levels (Figure 1H). To examine the performance in a hippocampus-dependent learning task, we analyzed *CK*Nrg1*$^{f/f}$ mutants in a cued and contextual fear-conditioning paradigm. *CK*Nrg1*$^{f/f}$ mutants showed a tendency for reduced contextual fear conditioning at 3 to 4 months (Figure 1I) and exhibited a reduced freezing response both to the context and the auditory cue at 12 months of age (Figure 1J). Thus, loss of NRG1 signaling results in progressive deficits in hippocampus-dependent learning.

Loss of NRG1 Signaling Disrupts Synaptic Plasticity and Alters the Balance of Excitatory-Inhibitory Neurotransmission in the Hippocampus

To address whether reduced fear-conditioned learning in *CK*Nrg1*$^{f/f}$ mutants might result from impaired LTP, we tested field excitatory postsynaptic potentials (fEPSPs) at the Schaffer collateral (SC)-CA1 synapse of acute hippocampal slices from 18- to 20-month-old *CK*Nrg1*$^{f/f}$ mutant and *Nrg1*$^{f/+}$ control mice. No change in the input-output curve was observed (data not shown), but paired-pulse facilitation was reduced in *CK*Nrg1*$^{f/f}$ mutants (Figure 2A). Next, we induced synaptic potentiation in CA1 by high-frequency stimulation (HFS) of the SC. Short-term potentiation (STP) (1 min after HFS) was reduced, and the magnitude of LTP remained depressed 60 min after induction in *CK*Nrg1*$^{f/f}$ mutants (Figure 2B). To examine whether disrupted LTP was associated with changes in synaptic transmission already at younger age, we performed whole-cell patch-clamp recordings in CA1 pyramidal neurons. In 3-month-old *CK*Nrg1*$^{f/f}$ mutants, the amplitude of spontaneous excitatory postsynaptic currents (sEPSCs) was decreased (Figures 2C and 2D). Conversely, the amplitude of spontaneous inhibitory postsynaptic currents (sIPSCs) was increased (Figures 2F and 2G). Both sEPSC and sIPSC frequency were unchanged (Figures 2C, 2E, 2F, and 2H). In addition, the amplitude and frequency of miniature EPSCs (mEPSCs) were depressed in *CK*Nrg1*$^{f/f}$ mutants (Figures 2I–2K), whereas mIPSC amplitude was enhanced (Figures 2L and 2M) and mIPSC frequency was depressed (Figures 2L and 2N). In summary, postnatal NRG1 deficiency in projection neurons shifts the balance of excitatory-inhibitory neurotransmission toward enhanced inhibition and leads to reduced LTP in the hippocampus at later stages.

Embryonic NRG1 Signaling Is Not Essential for Interneuron Migration and the Formation of Inhibitory Cortical Circuits

To identify NRG1 functions during the establishment of neuronal circuits, we performed a subset of the above

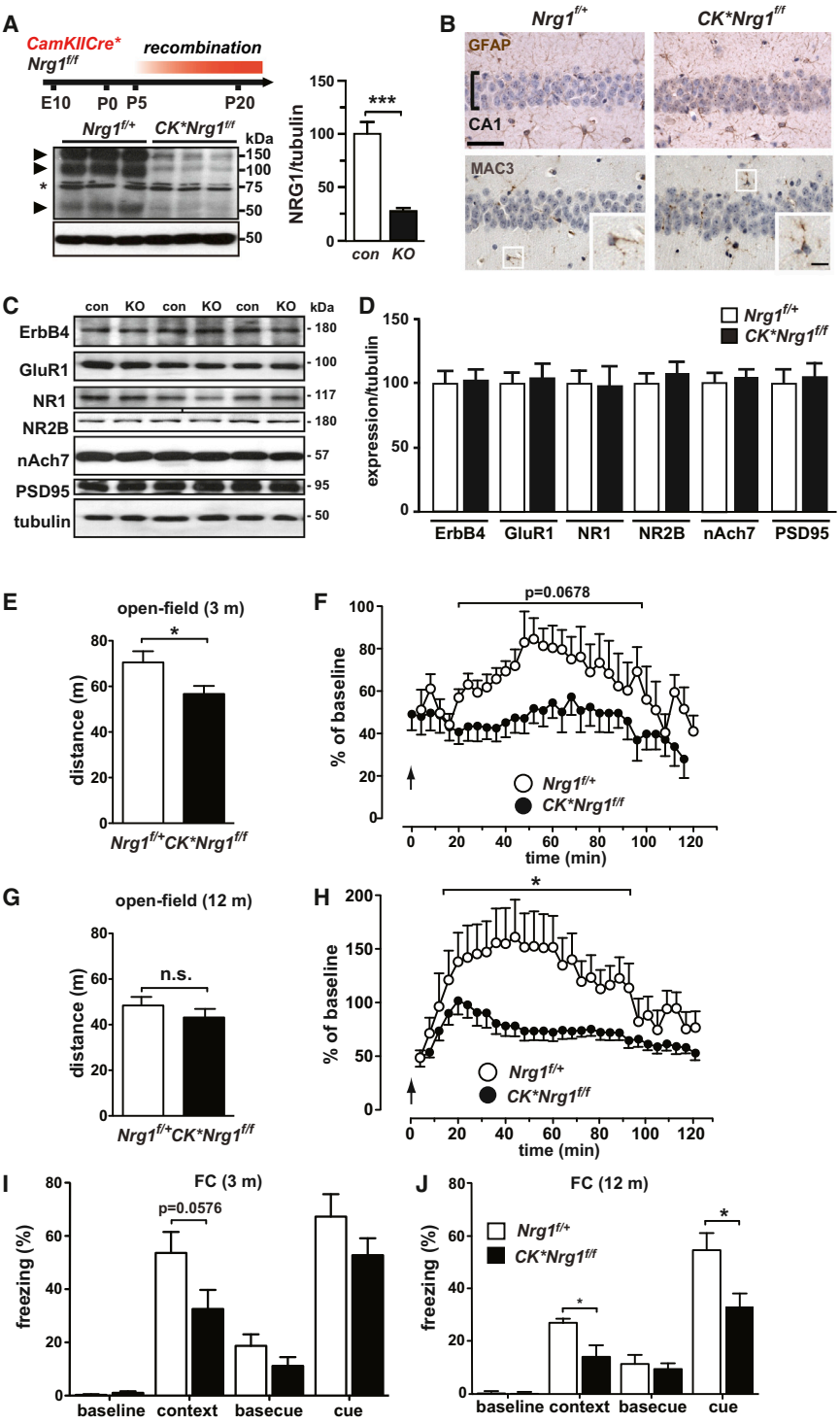

Figure 1. Behavioral Deficits in Mouse Mutants with a Postnatal Loss of NRG1 in Cortical Projection Neurons

(A) Time course of *Cre*-mediated NRG1 elimination in cortical projection neurons of *CamKCre*Nrg1*$^{f/f}$ mutants. (Left) Western blot analysis of cortical protein lysates from mutants (*CK*Nrg1*$^{f/f}$) and controls (*Nrg1*$^{f/+}$; age 15 months). Arrowheads, full-length CRD-NRG1 (~140 kDa), Ig-NRG1 (~95 kDa), and C-terminal processing product (~60 kDa). Asterisk, unspecific protein band. (Right) Densitometric quantification of 140, 95, and 60 kDa NRG1 bands. Integrated density values were normalized to β-tubulin (n = 3/genotype; ***p < 0.0001).

(B) Immunostaining of *CK*Nrg1*$^{f/f}$ mutants (12 months) shows absence of markers of inflammatory astrogliosis (GFAP) and microgliosis (MAC3) in the CA1 region (brackets). The scale bars represent 50 μm and 10 μm (inset).

(C) Western blot analysis of hippocampal protein lysates from *CK*Nrg1*$^{f/f}$ mutants (knockout [KO]) and *Nrg1*$^{f/+}$ controls (con) at 15 months after MK-801 treatment. ErbB4, ErbB4 receptor; GluR1, AMPA receptor subunit 1; NR1, NR2B, NMDA receptor subunit 1 and 2B; nAch7, nicotinic acetylcholine receptor α7 subunit; PSD95, postsynaptic density protein 95. β-tubulin was used as a loading control.

(D) Densitometric quantification of integrated density values normalized to β-tubulin (n = 3/genotype).

(E) Reduced motor activity of *CK*Nrg1*$^{f/f}$ mutants (n = 15) in the open-field test compared with *Nrg1*$^{f/+}$ controls (n = 10) at 3 months (*p < 0.05).

(F) Tendency for reduced responsiveness to MK-801 in *CK*Nrg1*$^{f/f}$ mutants compared with *Nrg1*$^{f/+}$ controls at 3 to 4 months. Motor activity in the open field was measured as the distance traveled during 4 min time intervals and expressed as percentage relative to baseline activity obtained individually before MK-801 treatment (single dose at 0.3 mg/kg). Arrow indicates MK-801 injection (*CK*Nrg1*$^{f/f}$ n = 9; *Nrg1*$^{f/+}$ n = 6; effect of genotype, p = 0.0678; two-way ANOVA for repeated measures).

(G) Unchanged motor activity of *CK*Nrg1*$^{f/f}$ mutants (age 12 to 13 months) in the open-field test (n = 9–13). n.s., not significant.

(H) Reduced MK-801-induced hyperactivity in *CK*Nrg1*$^{f/f}$ mutants compared with *Nrg1*$^{f/+}$ controls at 12 to 13 months (n = 9–13; significant effect of genotype, $F_{(2,\ 696)} = 5.43$, *p < 0.05; significant effect of time, $F_{(29,\ 696)} = 7.08$, ***p < 0.0001; two-way ANOVA for repeated measures).

(I) Tendency for reduced contextual fear conditioning in *CK*Nrg1*$^{f/f}$ mice in comparison to *Nrg1*$^{f/+}$ controls at 3 to 4 months (n = 9–11; p = 0.0576). Fear-conditioned learning is displayed as the percentage of time mice show freezing behavior during a 2 min time period after re-exposure to context or cue (tone). Baseline: freezing during initial exposure to context prior to cue exposure. Base cue: freezing during exposure to new context prior to cue re-exposure. FC, fear conditioning.

(J) Reduced contextual and cued fear conditioning in *CK*Nrg1*$^{f/f}$ mutant mice at 12 to 13 months (n = 9–12; *p < 0.05). Error bars represent SEM.

experiments in *Emx1-Cre*Nrg1*$^{f/f}$ mutants (*Emx*Nrg1*$^{f/f}$), in which NRG1 is eliminated in projection neurons and glial cells beginning at embryonic day (E) 10 (Figure 3A; Gorski et al., 2002). *Emx*Nrg1*$^{f/f}$ mutants were born at the expected Mendelian frequency and survived into adulthood. Despite a reduction of cortical NRG1 protein levels by ~80% in *Emx*Nrg1*$^{f/f}$

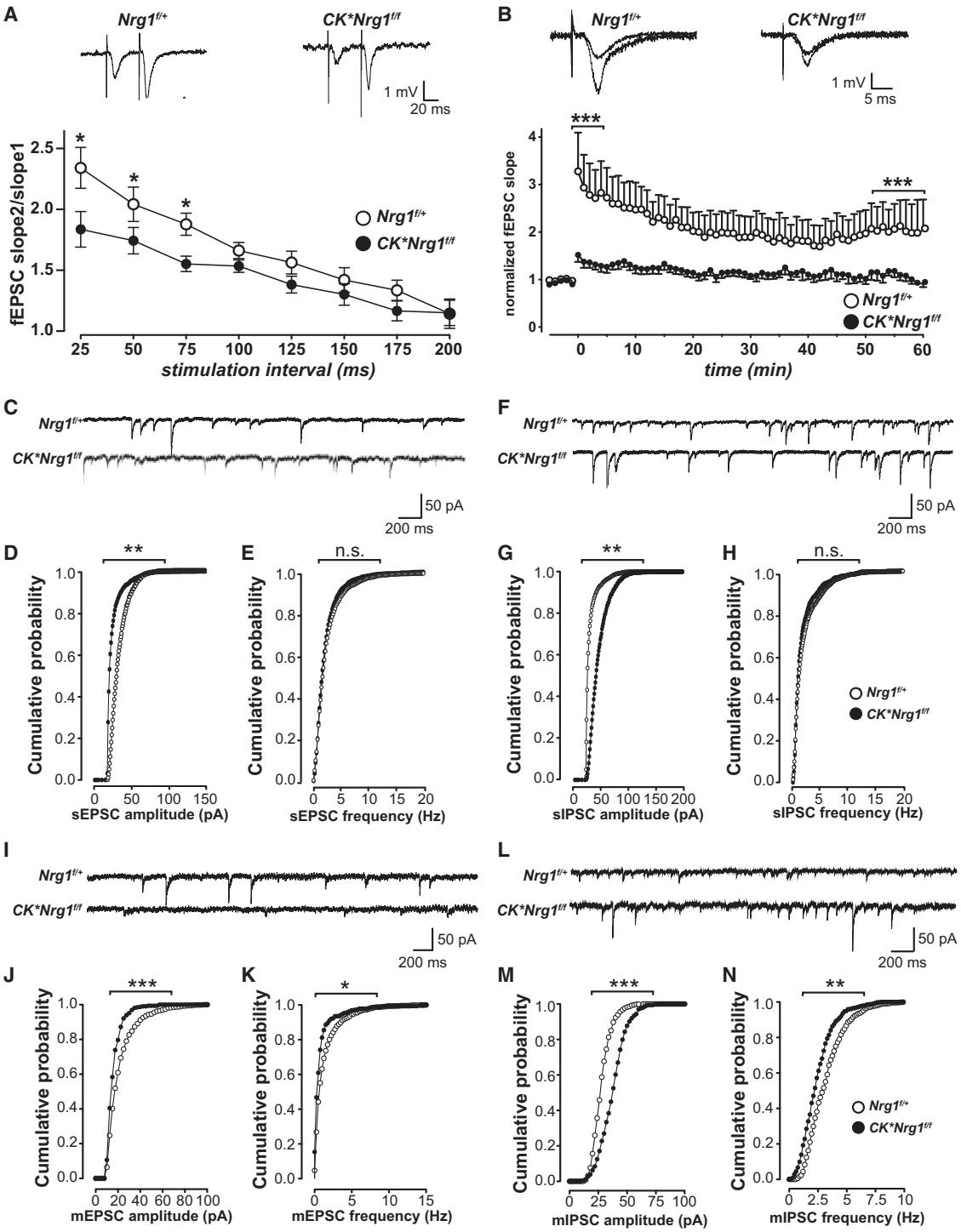

Figure 2. NRG1 Deficiency in Cortical Projection Neurons Disrupts Hippocampal Synaptic Plasticity and Increases Inhibitory Neurotransmission

(A) Top, sample fEPSPs traces from *CK*Nrg1*$^{f/f}$ mutant and *Nrg1*$^{f/+}$ control mice. Bottom, paired-pulse ratio (fEPSP slope second stimulus/fEPSP slope first stimulus) at interstimulus intervals of 25–75 ms was reduced in *CK*Nrg1*$^{f/f}$ mutants (n = 12) in comparison to *Nrg1*$^{f/+}$ controls (n = 11).

(B) Top, sample traces of responses before and after HFS. Bottom, LTP elicited by HFS (fEPSP slopes) for *CK*Nrg1*$^{f/f}$ mutants (n = 11) and *Nrg1*$^{f/+}$ controls (n = 12). HFS application at time point 0. Both the magnitude of STP (maximal responses within 1 min after HFS) and LTP (responses 50–60 min after HFS) were reduced in *CK*Nrg1*$^{f/f}$ mice.

(C) Representative sEPSC recordings from CA1 pyramidal neurons of a *CK*Nrg1*$^{f/f}$ mutant and *Nrg1*$^{f/+}$ control.

(legend continued on next page)

mutants (Figure 3B), gray and white matter structures appeared to be normally developed (Figures S2A and S2C). In contrast to ErbB4 mutants (Neddens and Buonanno, 2010), the number of GAD67-positive cells in the hippocampus (Figures 3C and 3E) and their cortical-layer-specific distribution (Figures 3D, 3F, and S2D) were not altered in *Emx*Nrg1*$^{f/f}$ mutants at postnatal day (P) 14.

Whole-cell patch-clamp recordings of CA1 pyramidal neurons revealed changes in neurotransmission in 3-month-old *Emx*Nrg1*$^{f/f}$ mutants similar to findings in *CK*Nrg1*$^{f/f}$ mutants. The amplitude of sEPSCs was depressed (Figures 3G–3I), whereas both sIPSC amplitude and frequency (***$p < 0.001$) were increased in *Emx*Nrg1*$^{f/f}$ mutants (Figures 3J–3L). Similarly, mEPSC amplitude was reduced (Figures 3M–3O) and mIPSC amplitude enhanced in *Emx*Nrg1*$^{f/f}$ mutants (Figures 3P–3R).

These findings argue against an essential role for glial and projection neuron-derived NRG1 during interneuron migration and the formation of inhibitory cortical circuits but support NRG1 functions in the fine tuning of excitatory and inhibitory neurotransmission in projection neurons.

Elevated CRD-NRG1 Expression Increases Inhibitory Neurotransmission and Disrupts Synaptic Plasticity in the Hippocampus

CRD-NRG1 is the most prominent NRG1 variant in the mature cortex (Liu et al., 2011). To test the hypothesis that CRD-NRG1 serves as a signal for ErbB-receptor-mediated synaptic tuning, we examined transgenic mice (*Nrg1-tg*) that express CRD-NRG1 from the neuronal Thy1.2 promoter (Michailov et al., 2004). Transgene expression was initiated around E16 (Figure S2B) and prominent in neocortex and hippocampus of the adult brain (Figures 4A and 4B). CRD-NRG1 accumulated on the surface of projection neurons but was absent from interneurons, astrocytes, and oligodendrocytes (Figure 4C). Western blot analysis revealed increased steady-state levels of phosphorylated ErbB4 receptor in the hippocampus of *Nrg1-tg* mice at 4 months of age (Figure 4D). Thus, *Nrg1-tg* mice model chronically elevated CRD-NRG1 expression (derived from cortical projection neurons) and ErbB4 receptor hyperphosphorylation beginning at late embryonic stages.

In the absence of markers of neurodegeneration and inflammation (Figure S2C), we performed in vivo MRI and found that lateral ventricular volume was reduced in *Emx*Nrg1*$^{f/f}$ mutants and increased in *Nrg1-tg* mice, whereas total brain volume was not changed at 12 months of age (Figures 4E–4G and S3F). Ventricular volume was already increased in 6-month-old *Nrg1-tg* mice (Figures S3C–S3E), but not at P14 (Figures S3A and S3B), suggesting a young adult onset. Thus, ventricular enlargement, a condition frequently observed in schizophrenia patients, is associated with elevated CRD-NRG1 expression, but not with NRG1 deficiency in our mouse models.

Next, we studied synaptic transmission in CA1 pyramidal neurons of *Nrg1-tg* mice and wild-type littermate controls (wild-type [*WT*]). Both sEPSC amplitude and frequency were unaltered in *Nrg1-tg* mice (Figures 5A–5C). In contrast, sIPSC frequency was almost doubled in *Nrg1-tg* mice (Figures 5D–5F). Similarly, mEPSC amplitude and frequency were unaltered (Figures S4A and S4B), whereas mIPSC frequency was enhanced in *Nrg1-tg* mice (Figures 5G and 5H). When we examined LTP at the SC-CA1 synapse, we observed no changes in the input-output curve or paired-pulse facilitation (Figure S4C); however, both STP and LTP were reduced in *Nrg1-tg* mice (Figure 5I). These findings suggest that elevated CRD-NRG1 signaling shifts the excitatory-inhibitory synaptic balance in CA1 pyramidal neurons toward enhanced inhibition, most likely due to increased synaptic input from GABAergic interneurons and/or enhanced presynaptic GABA release.

To address whether impaired LTP was related to changes in the molecular composition of cortical synapses, we prepared cortical synaptosomes from *Nrg1-tg* mice, *Emx*Nrg1*$^{f/f}$ mutants, and controls. Western blot analyses identified differences in the synaptic levels of CRD-NRG1 in *Nrg1-tg* mice in comparison to *Emx*Nrg1*$^{f/f}$ mutant mice, but protein levels for ErbB4, PSD95, as well as GluN1 and GluN2B subunits of NMDA receptors were not changed (Figures 5J and S5A), consistent with the unaltered transcription of ErbB4 and various neurotransmitter receptors (Figures S5B–S5E). To obtain global protein expression profiles from *Nrg1-tg* mice, we analyzed their proteome using a label-free shotgun-liquid chromatography-mass spectrometry (LC-MS^{E}) approach. This resulted in the identification of 40 differentially expressed proteins in the hippocampus of 4-month-old *Nrg1-tg* mice (see Table S1), including several that play a role in functional and structural plasticity at glutamatergic synapses (CaM kinase II α and β subunits, protein phosphatase 2B, and septin 6; Figure 5K). Next, we identified interaction networks and canonical pathways using the Ingenuity Pathways KnowledgeBase (IPKB) (http://www.ingenuity.com). A significant network showed interactions of the uploaded proteins with a cluster of glutamate receptors (Figure 5L; Table S2). The most significant canonical pathway was LTP (not shown; $p < 0.001$), consistent with our electrophysiological findings in *Nrg1-tg* mice.

(D and E) Cumulative probability plots of sEPSC amplitude (D) and frequency (E) in CA1 pyramidal neurons from *CK*Nrg1*$^{f/f}$ mutants (n = 6) and *Nrg1*$^{f/+}$ controls (n = 8).
(F) Representative sIPSC recordings from CA1 pyramidal neurons of a *CK*Nrg1*$^{f/f}$ mutant and *Nrg1*$^{f/+}$ control.
(G and H) Cumulative probability plots of sIPSC amplitude (G) and frequency (H) in CA1 pyramidal neurons from *CK*Nrg1*$^{f/f}$ mutant (n = 8) and *Nrg1*$^{f/+}$ control (n = 5) mice.
(I) Representative mEPSC recordings from CA1 pyramidal neurons of a *CK*Nrg1*$^{f/f}$ mutant and *Nrg1*$^{f/+}$ control.
(J and K) Cumulative probability plots of mEPSC amplitude (J) and frequency (K) in CA1 pyramidal neurons from *CK*Nrg1*$^{f/f}$ mutants (n = 6) and *Nrg1*$^{f/+}$ controls (n = 8).
(L) Representative mIPSC recordings from CA1 pyramidal neurons of a *CK*Nrg1*$^{f/f}$ mutant and *Nrg1*$^{f/+}$ control.
(M and N) Cumulative probability plots of sIPSC amplitude (M) and frequency (N) in CA1 pyramidal neurons from *CK*Nrg1*$^{f/f}$ mutant (n = 9) and *Nrg1*$^{f/+}$ control (n = 10) mice. *$p < 0.05$; **$p < 0.01$; ***$p < 0.001$; Mann-Whitney U test.

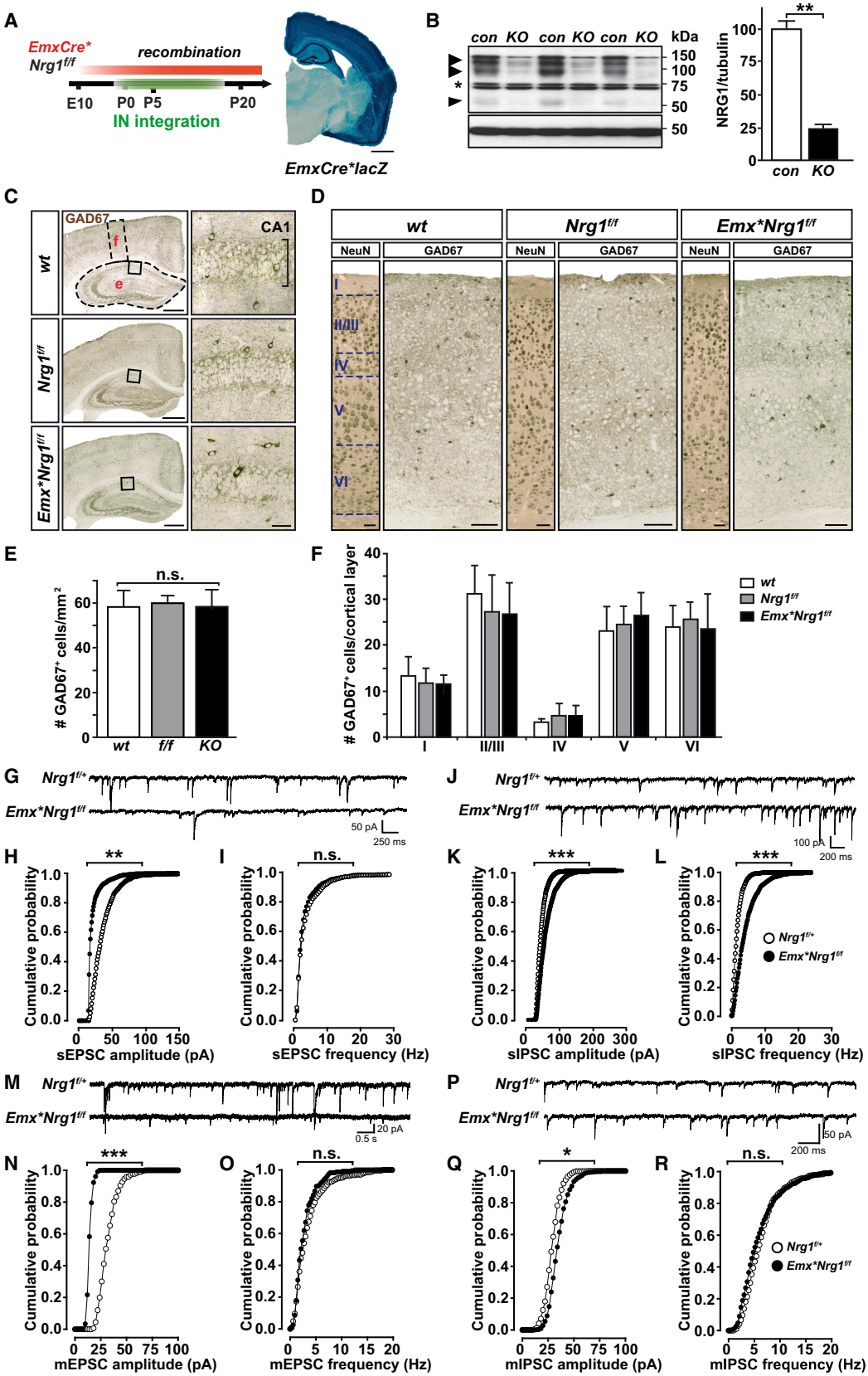

(legend on next page)

Abnormal Spine Growth and Reduced Numbers of Parvalbumin-Expressing Interneurons in the Neocortex of *Nrg1-tg* Mice

We next addressed whether increased CRD-NRG1 expression also affects neocortical network functions. To visualize dendrites and spines, we crossbred *Nrg1-tg* mice with a *Thy1.2-YFP* transgenic mouse line, which expresses yellow fluorescent protein (YFP) in a subset of projection neurons in cortical layer V (Hirrlinger et al., 2005). In vivo imaging of dendrites in *Thy1.2-YFP*Nrg1-tg* double transgenic mice (*YFP*Nrg1*) and *Thy1.2-YFP* controls (con) at 3 to 4 months of age by two-photon laser-scanning microscopy (2P-LSM) revealed no difference in the number of primary dendrites (*con:* 7.24 ± 0.17; *YFP*Nrg1:* 7.18 ± 0.09; Figures 6A, 6B, and S6C) and branch points of apical dendrites up to the marginal zone (MZ) (*con:* 4.03 ± 0.32; *YFP*Nrg1:* 4.23 ± 0.22; Figures 6A and 6C). Next, we applied stimulated emission depletion (STED) nanoscopy through a cranial window above the somatosensory cortex to resolve structural details of apical dendrites and spines of layer V projection neurons in the MZ of live mice (Berning et al., 2012). Total spine frequency was not changed in *YFP*Nrg1* mice (*con:* 0.35 ± 0.02 μm^{-1}, *YFP*Nrg1:* 0.36 ± 0.02 μm^{-1}; Figure 6D). Using in vivo STED nanoscopy, we observed several previously defined morphological spine classes ("mushroom," "cup," "stubby," "filopodium," and "bifurcated"; Hering and Sheng, 2001; Trommald et al., 1996) and determined their frequency (Figures S6A and S6B). In *YFP*Nrg1* mice, the frequency of bifurcated spines was increased more than 3-fold (*con*: set as 1 ± 0.31; *YFP*Nrg1*: 3.74 ± 0.82; $p < 0.01$), and we observed a concomitant, albeit not significant, reduction in the frequency of other spine types, except for filopodium-like spines (Figure 6E). Furthermore, the necks of mushroom and cup spines were longer in *YFP*Nrg1* mice compared with controls (*mushroom*: *con*: 0.98 ± 0.04 μm, *YFP*Nrg1*: 1.2 ± 0.05 μm, $p < 0.05$; *cup*: *con*: 1.05 ± 0.06 μm, *YFP*Nrg1*: 1.27 ± 0.02 μm, $p < 0.05$; Figure 6F).

To assess functional consequences of the selective increase of bifurcated spines, we performed recordings in cortical layer V neurons using acute cortical slices prepared from the same neocortical area that was used for in vivo STED nanoscopy. Both mEPSC frequency and amplitude were increased in *YFP-Nrg1* mice (Figures 6G–6I). In addition, analysis of mEPSC kinetics revealed that the mean slope of onset was increased and the distribution shifted toward events with faster onset in *YFP-Nrg1* mice (*con*: 12.77 ± 0.23 pA/ms; *YFP-Nrg1*: 18.24 ± 0.26 pA/ms; Figure 6J). Given that perisomatic events display faster onset in comparison to dendritic events (Miles et al., 1996), these data suggest that changes in spine structure may reduce effective glutamatergic synaptic transmission by changing the NMDA/AMPA ratio or postsynaptic receptor kinetics at distal sites.

CRD-NRG1 serves as a permissive signal for the migration of cortical interneurons in vitro (Flames et al., 2004), suggesting that interneuron migration could be affected in *Nrg1-tg* mice. Immunostaining for GAD67 and parvalbumin (PV) at P14 revealed minor changes in the cortical distribution of $GAD67^+$ cells in *Nrg1-tg* mice (Figure 7A), but not in the total number of neocortical (Figures 7A and 7B) and hippocampal interneurons (Figures S6D and S6E). To visualize PV^+ interneurons in vivo, we crossbred *Nrg1-tg* mice with *PV-GFP* transgenic mice that express GFP under control of regulatory sequences from the *PV* gene (Meyer et al., 2002). 2P-LSM in vivo imaging of *PV-GFP*Nrg1-tg* double transgenic mice at 3 months of age revealed a lower number of GFP^+ cells in cortical layers II/III and V and a reduction in the total number of GFP^+ cells by ~20% compared with *PV-GFP* controls (Figures 7C and 7D). We observed a similar reduction of GFP^+ cells in a second mouse line, which expresses epitope-tagged CRD-NRG1 (Velanac et al., 2012). PV^+

Figure 3. Embryonic NRG1 Signaling Is Not Essential for Interneuronal Migration

(A) Embryonic NRG1 elimination using the *Emx1-Cre* driver line overlaps with network integration of cortical interneurons (IN). X-gal histochemistry on brain section from an *Emx-Cre*Rosa26lacZ* double-transgenic mouse (P46) shows Cre-mediated recombination of *lacZ* reporter in forebrain projection neurons and glial cells. The scale bar represents 1 mm.

(B) (Left) Western blot analysis of cortical protein extracts from *Emx*Nrg1$^{f/f}$* mutants (KO) and *Nrg1$^{f/+}$* con at 4 months. Arrowheads, full-length and processed NRG1 protein. Asterisk, unspecific protein band. (Right) Densitometric quantification of NRG1 isoforms (140 and 95 kDa). Integrated density values were normalized to β-tubulin (n = 3/genotype; $^{**}p < 0.01$).

(C) Normal numbers and cortical positions of $GAD67^+$ interneurons in *Emx*Nrg1$^{f/f}$* mutants during cortical maturation. Immunostaining for GAD67 on coronal brain sections from *Emx*Nrg1$^{f/f}$* mutants and controls (*Nrg1$^{f/f}$* and *WT*) at P14. Higher magnifications (right) show the hippocampal CA1 region (boxed in overviews). The scale bars represent 500 μm and 50 μm (CA1 region).

(D) Immunostaining for NeuN and GAD67 (higher magnification of boxed area f in C) reveals normal layering (I–VI, cortical layers) and interneuron positions in the somatosensory cortex of *Emx*Nrg1$^{f/f}$* mutants in comparison to controls (*Nrg1$^{f/f}$* and *WT*). Bregma, −1.7; scale bars, 50 μm (NeuN); 100 μm (GAD67).

(E) Quantification of $GAD67^+$ interneurons in the hippocampus (marked area e in C) of *Emx*Nrg1$^{f/f}$* mutants and controls (*Nrg1$^{f/f}$* and *WT*). n = 6/genotype.

(F) Quantification of $GAD67^+$ interneurons in the neocortex (boxed area f in C) of *Emx*NRG1$^{f/f}$* mutants and controls (*Nrg1$^{f/f}$* and *WT*). n = 6/genotype. Error bars represent SEM.

(G) Representative sEPSC recordings of CA1 pyramidal neurons from *Emx*NRG1$^{f/f}$* mutants and *Nrg1$^{f/+}$* controls.

(H and I) Cumulative probability plots of sEPSC amplitude (H) and frequency (I) in CA1 pyramidal neurons from *Emx*Nrg1$^{f/f}$* mutants (n = 9) and *Nrg1$^{f/+}$* controls (n = 8).

(J) Representative sIPSC recordings of pyramidal neurons from *Emx*NRG1$^{f/f}$* mutants and *Nrg1$^{f/+}$* controls.

(K and L) Cumulative probability plots of sIPSC amplitude (K) and frequency (L) in pyramidal neurons from *Emx*Nrg1$^{f/f}$* mutants (n = 6) and *Nrg1$^{f/+}$* controls (n = 7).

(M) Representative mEPSC recordings of pyramidal neurons from *Emx*NRG1$^{f/f}$* mutants and *Nrg1$^{f/+}$* controls.

(N and O) Cumulative probability plots of mEPSC amplitude (N) and frequency (O) in pyramidal neurons from *Emx*Nrg1$^{f/f}$* mutants (n = 8) and *Nrg1$^{f/+}$* controls (n = 5).

(P) Representative mIPSC recordings of pyramidal neurons from *Emx*NRG1$^{f/f}$* mutants and *Nrg1$^{f/+}$* controls.

(Q and R) Cumulative probability plots of mIPSC amplitude (Q) and frequency (R) in pyramidal neurons from *Emx*Nrg1$^{f/f}$* mutants (n = 10) and *Nrg1$^{f/+}$* controls (n = 10).

$^{*}p < 0.05$; $^{**}p < 0.01$; $^{***}p < 0.001$; Mann–Whitney U test.

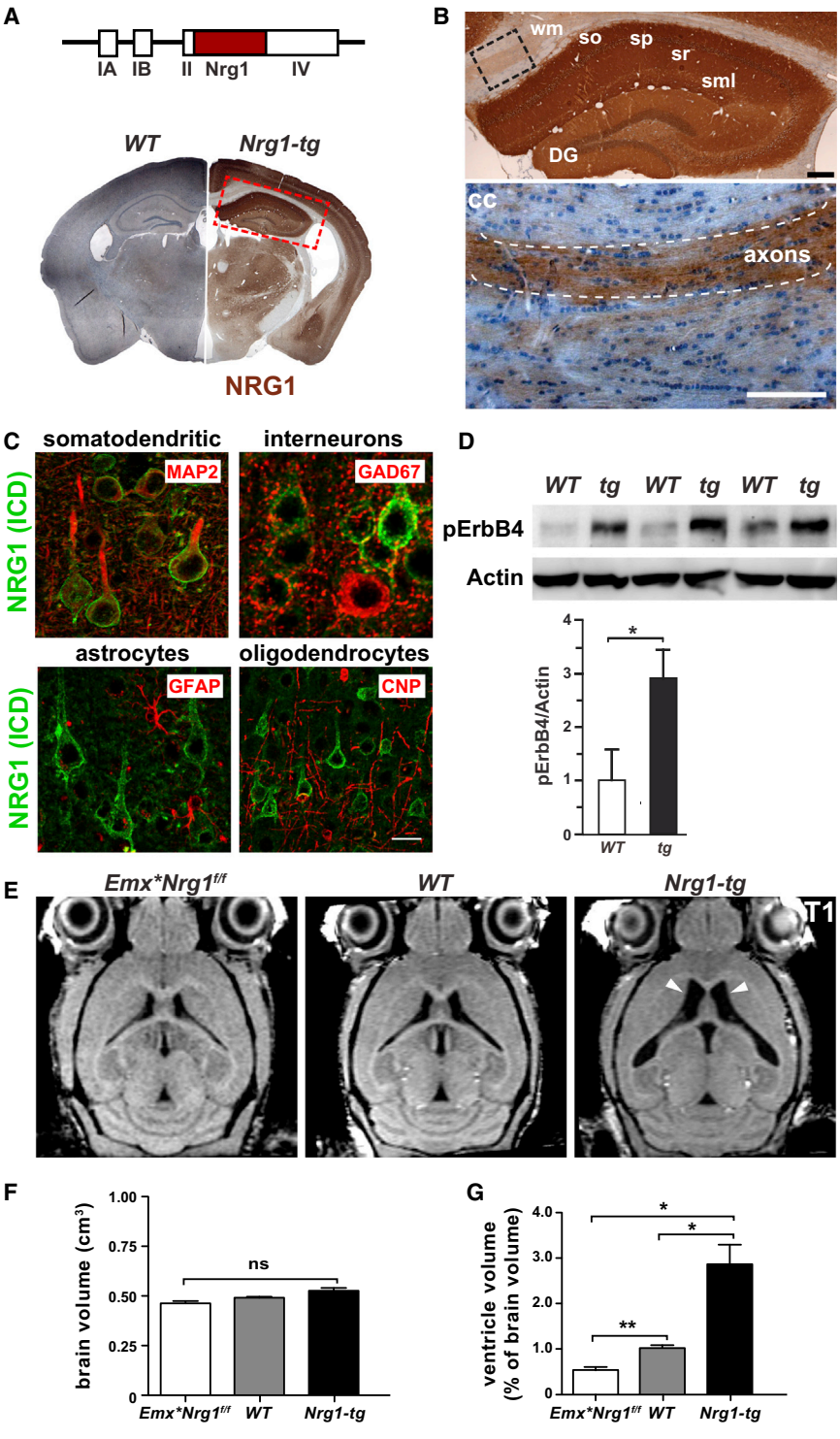

Figure 4. Elevated CRD-NRG1 Expression Causes Ventricular Enlargement

(A) Neuronal CRD-NRG1 overexpression in transgenic mice. Structure of the Thy1.2 transgene cassette (brown box, CRD-NRG1 cDNA; white boxes, exons I-IV of the Thy1.2 gene). Immunostaining for NRG1 on coronal brain sections from wild-type (*WT*) and CRD-NRG1 transgenic mice (*Nrg1-tg*) at 12 months. Note enlarged lateral ventricle in *Nrg1-tg* brain.

(B) Top, CRD-NRG1 expression in hippocampal pyramidal neurons and granule cells of *Nrg1-tg* mice (magnification of boxed area in A). Bottom, CRD-NRG1 is present in callosal axons (magnification of boxed area at the top). cc, corpus callosum; DG, dentate gyrus; sml, stratum moleculare; so, stratum oriens; sp, stratum pyramidale; sr, stratum radiatum; wm, white matter. The scale bars represent 125 μm (top) and 60 μm (bottom).

(C) Projection neuron-specific CRD-NRG1 overexpression. Confocal images of coronal brain sections after fluorescent immunostaining for NRG1 (green) and markers (red) for projection neurons (MAP2), interneurons (GAD67), astrocytes (GFAP), and oligodendrocytes (CNP) in the somatosensory cortex of *Nrg1-tg* mice. The scale bar represents 20 μm.

(D) Chronic ErbB4 hyperphosphorylation in the hippocampus of *Nrg1-tg* mice. Western blot analysis of hippocampal protein lysates from *Nrg1-tg* mice (*tg*) and WT (4 months). Densitometric quantification of phosphorylated ErbB4 bands. Integrated density values were normalized to β-actin (n = 3/genotype; *$p < 0.05$; two-tailed t test).

(E) Enlarged lateral ventricles in *Nrg1-tg* mice (arrowheads) in comparison to *Emx*Nrg1*$^{f/f}$ mutants and *WT* mice (12 to 13 months). T1-weighted MRI.

(F) MRI-based volumetric analysis reveals no changes in total brain volume (cm^3) of *Emx*Nrg1*$^{f/f}$ mutants and *Nrg1-tg* in comparison to *WT* mice (n = 5 per genotype; Mann-Whitney U test).

(G) Ventricular volume (in percent of total brain volume) is reduced in *Emx*Nrg1*$^{f/f}$ mutants and increased in *Nrg1-tg* in comparison to *WT* mice (*WT, Emx*Nrg1*$^{f/f}$, n = 5; *Nrg1-tg,* n = 4; **$p < 0.01$, WT versus *Emx*Nrg1*$^{f/f}$; $p < 0.05$, *WT* versus *Nrg1-tg* and *Emx*f/f* versus *Nrg1-tg*; Mann-Whitney U test).

interneurons provide perisomatic inhibition to projection neurons. Electrophysiological recordings in acute cortical slices (as above) revealed a moderate increase in mIPSC frequency in layer V projection neurons (Figures 7E–7G). Analysis of mIPSC kinetics showed a shift toward events with slower onset, such that the mean slope of event onset was reduced in *Nrg1-tg* mice (con: 27.9 ± 0.34 pA/ms; *Nrg1-tg*: 22.8 ± 0.18 pA/ms; Figure 7H), consistent with a reduction of PV^+ interneuron-mediated perisomatic events in layer V.

Finally, we tested whether increased CRD-NRG1 expression causes behavioral dysfunctions. The neuromuscular junction in *Nrg1-tg* mice is severely compromised (W.J. Thompson, personal communication), which renders these mice less suitable for behavioral analysis. Therefore, we examined a mouse line (*HA-Nrg1-tg*), in which hemagglutinin (HA) epitope-tagged CRD-NRG1 is expressed under control of the same Thy1.2 cassette as in *Nrg1-tg* mice

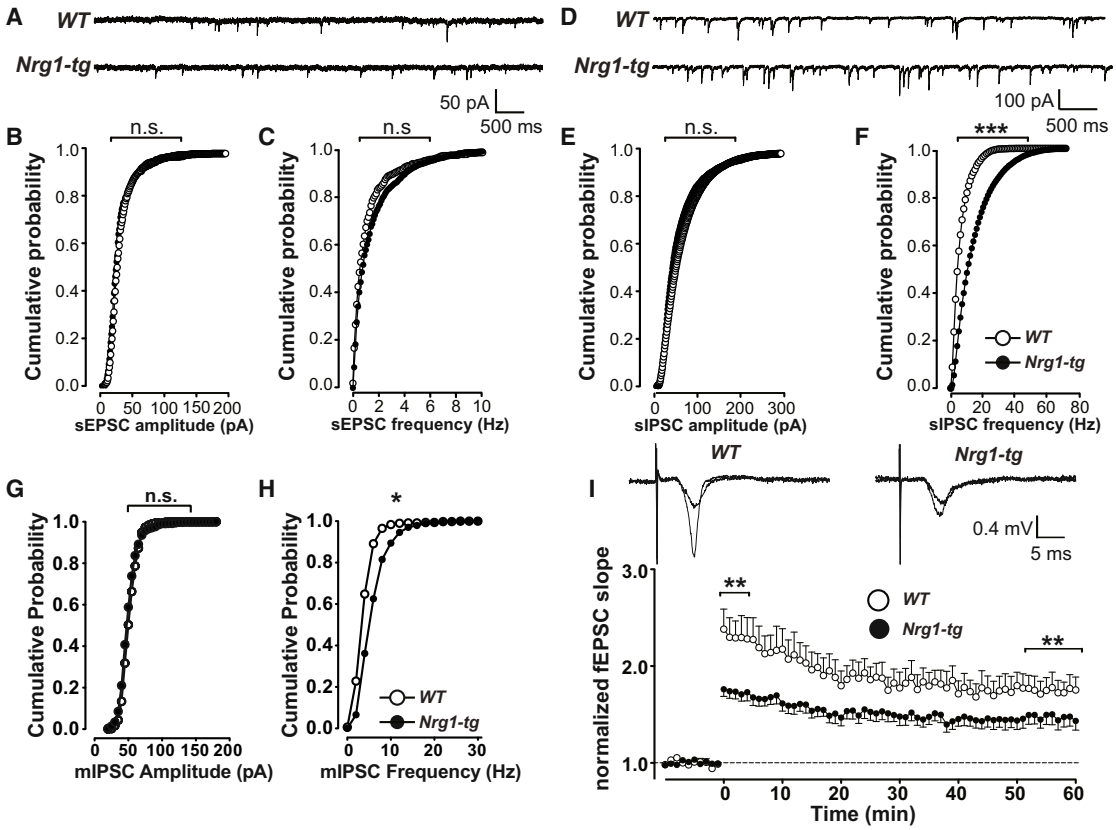

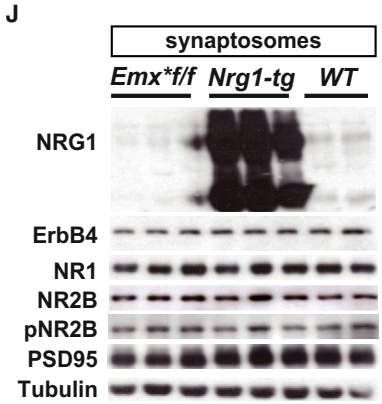

K

Acc	Protein	Ratio	Pep	Wilco
Cell signalling				
P11798	CaM kinase II alpha chain	0.67	51	0.0304
P28652	CaM kinase II beta chain	0.77	43	0.0304
P48454	Ser/Thr-protein phosphatase 2B	1.23	6	0.0141
P97813	Phospholipase D2	1.43	2	0.0304
Cytoskeleton/ECM				
Q9QYR6	Microtubule-associated protein 1A	1.10	37	0.0304
Q9R1T4	Septin 6	0.82	2	0.0464
Q99KJ8	Dynactin subunit 2	0.77	3	0.0102
Q62059	Versican core protein	0.80	2	0.0043
Ion transport				
Q924N4	Solute carrier family 12 member 6	1.15	19	0.0120
Q5DTL9	Na-driven Cl-bicarbonate exchanger	1.27	8	0.0262

L

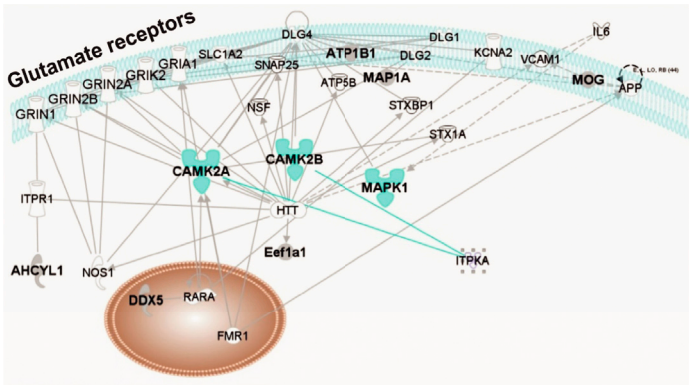

(legend on next page)

(Figure S7A; Velanac et al., 2012). Similar to *Nrg1-tg* mice, we observed HA-CRD-NRG1 expression on the surface of cortical projection neurons, ventricular enlargement, and a reduced number of GFP+ interneurons in *HA-Nrg1-tg* mice (Figures S7B–S7D). At 2 to 3 months of age, the distance traveled in the open-field test was not altered in *HA-Nrg1-tg* mice (m; males: *WT*: 44.17 ± 1.93, *HA-Nrg1-tg*: 42.49 ± 2.21; females: *WT*: 42.92 ± 1.41, *HA-Nrg1-tg*: 42.31 ± 2.32; Figure S7E). However, *HA-Nrg1-tg* mice spent less time in the center of the open-field arena (males: *WT*: 24.16% ± 3.77%, *HA-Nrg1-tg*: 10.61% ± 2.13%; females: *WT*: 21.11% ± 2.11%, *HA-Nrg1-tg*: 6.87% ± 2.41%; Figure 7I) and male mice displayed more frequent defecation (males: *WT*: 1.778 ± 0.586; *HA-Nrg1-tg*: 4.13 ± 0.72; Figure S7F), in line with increased anxiety. In addition, *HA-Nrg1-tg* mice performed fewer rearings (males: *WT*: 56.28 ± 3.86, *HA-Nrg1-tg*: 39 ± 4.64; females: *WT*: 48.5 ± 2.92, *HA-Nrg1-tg*: 31.1 ± 4.53; Figure 7J), suggesting diminished exploratory behavior. Assessment of sensorimotor gating (Figures 7K and 7L) showed a profound PPI deficit in *HA-Nrg1-tg* mice. Moreover, they displayed an increased startle response (males: *WT*: 184.9 ± 39.56, *HA-Nrg1-tg*: 344.9 ± 42.07; females: *WT*: 71.43 ± 12.51, *HA-Nrg1-tg*: 280.2 ± 19.24; Figure S7G). In summary, our findings in loss- and gain-of-function mouse mutants support a bell-shaped model of NRG1-mediated synaptic functions (Figure 8), according to which an optimal level of NRG1 signaling is required for balanced synaptic transmission and plasticity in the cortex.

DISCUSSION

In this study, we carried out a systematic characterization of conditional *Nrg1* mutants and *Nrg1-tg* mice with increased CRD-NRG1 expression. The main findings of this study are as follows: (1) Both NRG1 deficiency and increased CRD-NRG1 expression led to disrupted hippocampal plasticity and imbalanced excitatory and inhibitory neurotransmission. (2) Elevated CRD-NRG1 expression resulted in ventricular enlargement and abnormal spine growth. (3) Morphological changes in *Nrg1-tg* mice were accompanied by increased anxiety levels and disrupted sensorimotor gating.

Our analysis of *CK*Nrg1*$^{f/f}$ mutants has shown that NRG1 is required for hippocampal LTP. This finding contrasts with a study in heterozygous *Nrg1* mutants, in which hippocampal LTP was increased (Shamir et al., 2012). These discrepancies most likely reflect differences in the spatiotemporal profile of *Nrg1* deletion in conventional heterozygous mutants in comparison to conditional *Nrg1*-null mutants and point to the modulatory role of distinct levels of NRG1 during synaptic transmission. In addition, loss of NRG1 in *CK*Nrg1*$^{f/f}$ and *Emx*Nrg1*$^{f/f}$ mutant mice consistently resulted in increased IPSC amplitudes in hippocampal pyramidal neurons. We conclude that expression or responsiveness of postsynaptic GABA receptors on pyramidal neurons is enhanced in the absence of NRG1 signaling. Our findings in *Nrg1* conditional mutants contrast with those in *ErbB4*-null mutants, in which inhibitory circuits are compromised (Del Pino et al., 2013; Fazzari et al., 2010; Neddens and Buonanno, 2010; Wen et al., 2010) and LTP is enhanced (Chen et al., 2010; Pitcher et al., 2008; Shamir et al., 2012). Thus, we suggest that NRG1 is an important, but not the sole, mediator of ErbB4 signaling in the brain and that ErbB4 integrates signals from multiple ligands, such as neuregulin 2 (Carraway et al., 1997), during the regulation of inhibitory circuits.

Similar to NRG1 deficiency, elevated CRD-NRG1 expression in projection neurons disrupted hippocampal LTP. In addition, we observed increased IPSC frequency and abnormal spine growth in pyramidal cells of CRD-NRG1 transgenic mice. These effects appeared to be specific for CRD-NRG1 as overexpression of Ig-domain-containing NRG1 (Ig-NRG1 or NRG1 type I) in transgenic mice using the same Thy1.2 promoter led to impaired gamma oscillation, whereas LTP formation was not affected (Deakin et al., 2012). A distinct transgenic mouse line with forebrain-specific overexpression of Ig-NRG1 shows reduced mEPSC frequency and mIPSC amplitudes but unaltered mIPSC frequency (Yin et al., 2013a). These data suggest that CRD-NRG1, mainly acting via juxtacrine signaling, and Ig-NRG1, serving as a soluble ligand in paracrine signaling, provide distinct functions in the modulation of excitatory and inhibitory neurotransmission. Together, our data demonstrate an imbalance in the excitatory/inhibitory (E/I) ratio toward pronounced inhibition in conditional *Nrg1* mutants and CRD-NRG1 transgenic mice. We speculate that alterations in the E/I ratio in response to altered NRG1 signaling could lead to deficits in cortical synchronization, as implicated in schizophrenia (Uhlhaas and Singer, 2010).

Figure 5. Elevated CRD-NRG1 Expression Increases Inhibitory Neurotransmission and Disrupts Hippocampal Plasticity

(A) Representative sEPSC recordings from CA1 pyramidal neurons in *WT* and *Nrg1-tg* mice (3 to 4 months).

(B and C) Cumulative probability plots of sEPSC amplitude (B) and frequency (C) in pyramidal neurons from *Nrg1-tg* mice (n = 15) compared with *WT* (n = 10).

(D) Representative sIPSC recordings from pyramidal neurons in *WT* and *Nrg1-tg* mice.

(E and F) Cumulative probability plots of sIPSC amplitude (E) and frequency (F) in pyramidal neurons from *WT* (n = 9) and *NRG1-tg* mice (n = 16).

(G and H) Cumulative probability plots of mIPSC amplitude (G) and frequency (H) in pyramidal neurons from *WT* (n = 8) and *NRG1-tg* mice (n = 9). *$p < 0.05$; **$p < 0.01$; ***$p < 0.001$; Mann-Whitney U test.

(I) Sample traces of responses (top) before and after HFS and LTP elicited by HFS. fEPSP slopes from *Nrg1-tg* mice (n = 22) were in comparison to *WT* mice (n = 15). Both STP and LTP were significantly reduced in *Nrg1-tg* mice (**$p < 0.01$; Student's t test).

(J) Western blot analysis of proteins (Triton X-100 soluble and insoluble fraction of synaptosomal lysates) prepared from cerebral cortices of *Emx*Nrg1*$^{f/f}$ mutant, *Nrg1-tg*, and *WT* mice (age 15–18 months). Levels of ErbB4, NR1, NR2B, phosphorylated NR2B (pNR2B), and PSD95 were unaltered in all genotypes. Note: β-tubulin cosediments in all fractions as a contaminant.

(K) LC-MS^E identification of differentially expressed proteins in the hippocampus of *Nrg1-tg* (n = 10) in comparison to *WT* (n = 10) mice. Acc, UniProt accession code; ECM, extracellular matrix; Pep, number of peptides identified for each protein; Ratio, *Nrg1-tg/WT* for each protein; Wilco, Wilcoxon test.

(L) Accession codes for altered proteins (see Table S1) were uploaded into the Ingenuity Pathways KnowledgeBase (IPKB). This led to identification of a significant network (score 15), which showed interactions of the uploaded proteins with other proteins in the IPKB (see Table S2). CAMK2A, CAMK2B, and mitogen-activated protein kinase 1 (MAPK1) kinases are highlighted in blue. A cluster of five glutamate receptors predicted to interact with the uploaded proteins is also indicated.

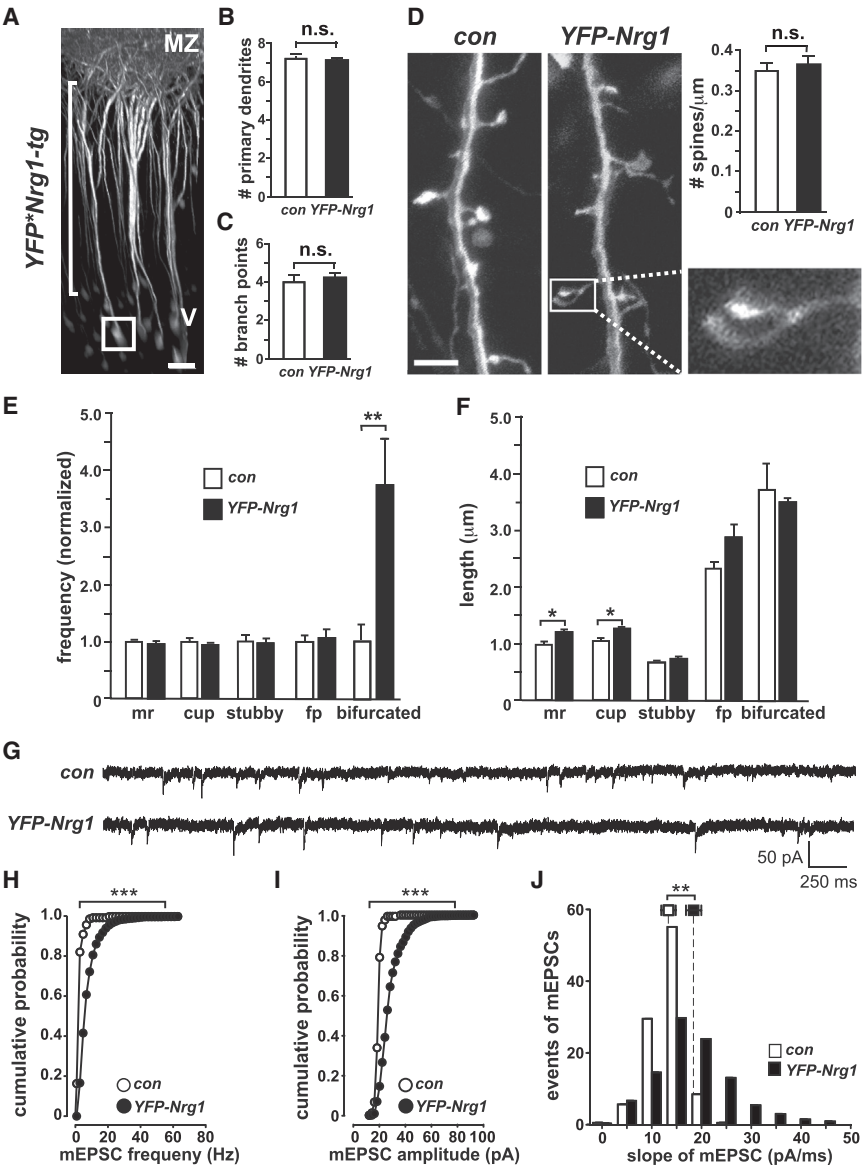

Figure 6. Abnormal Spine Growth in *Nrg1-tg* Mice

(A) 2P-LSM imaging of cortical layer V projection neurons. Fluorescent image stacks were recorded in *Thy1.2-YFP*Nrg1-tg* (*YFP-Nrg1*) and *Thy1.2-eYFP* (*con*) mice at 3 to 4 months. 3D volume of the somatosensory cortex (bregma −2) from the marginal zone (MZ) to layer V, rendered from fluorescent image stacks. Box and bracket indicate areas used for quantification in (B) and (C). The scale bar represents 40 µm.

(B) The number of primary dendrites (quantified in boxed area in A) was not altered in *YFP*Nrg1* compared with control mice (n = 10 neurons/mouse; n = 7 mice/genotype).

(C) The number of apical dendrite branch points (from cell soma in layer V to the MZ, indicated by bracket in A) was not altered in *YFP*NRG1* mice compared with control mice (n = 10 neurons/mouse; n = 7 mice/genotype).

(D) In vivo STED nanoscopy of dendrites in the MZ derived from cortical layer V projection neurons of a con and a *YFP*Nrg1* mouse. A bifurcated-type spine (boxed) is shown at higher magnification. The scale bar represents 2 µm.

(E) Relative frequency of spine classes (controls set as 1) in the MZ of *YFP-Nrg1* mice and controls (30 dendrites per mouse; con, n = 4 mice; *YFP-Nrg1*, n = 3, $^{**}p < 0.01$; one way ANOVA, post hoc Tukey's test). fp, filopodium; mr, mushroom.

(F) Length (µm) of spine neck (for mushroom, cup, and bifurcated spines) or entire spine (stubby and filopodium). Necks of mushroom- and cup-like spines were longer in *YFP-Nrg1* mice (30 dendrites/mouse; *con*, n = 4 mice; *YFP-Nrg1*, n = 3; $^{*}p < 0.05$; $^{**}p < 0.01$; one-way ANOVA; post hoc Tukey's test). Error bars represent SEM.

(G) Representative recordings of glutamatergic mEPSCs from YFP^+ projection neurons in cortical layer V of control and *YFP-Nrg1* mice.

(H and I) Cumulative probabilities of mEPSC frequencies (H) and amplitudes (I) in YFP^+ neurons from control (n = 12) and *YFP-Nrg1* (n = 13) mice. $^{**}p < 0.01$; $^{***}p < 0.001$; Mann-Whitney U test.

(J) Onset kinetics expressed as normalized histograms of rise slopes (peak amplitude in pA over time of onset in ms) of glutamatergic mEPSCs. Mean values and the significance of onset kinetics are indicated by squares positioned relative to the x axis. $^{**}p < 0.01$; Mann-Whitney U test.

Based on the phenotypic profile of CRD-NRG1 overexpressing mice, we suggest that human NRG1 risk haplotypes exert a gain-of-function effect. This hypothesis is supported by the finding that the schizophrenia risk haplotype HapICE is associated with increased CRD-NRG1 expression in the prefrontal cortex (Weickert et al., 2012). In addition, elevated CRD-NRG1 expression induced chronic ErbB4 hyperphosphorylation in the cortex of CRD-NRG1 transgenic mice, consistent with findings in postmortem brain from schizophrenia patients (Hahn et al., 2006). We propose that elevated CRD-NRG1 signaling impairs synaptic plasticity via two mechanisms. First, it alters the cortical E/I ratio. Specifically, we hypothesize that increased juxtacrine signaling by CRD-NRG1 during development hyperstimulates ErbB4 receptors in PV^+ interneurons, which increases feedforward inhibition by promoting the formation of GABAergic presynaptic terminals on pyramidal neurons, as indicated by elevated IPSC frequency. Increased feedforward inhibition could compromise LTP formation. Second, it induces abnormal spine growth. Elevated expression levels of CRD-NRG1 result in its accumulation in the somatodendritic compartment of pyramidal neurons. This could initiate abnormal backsignaling, such as aberrant interactions of the C-terminal domain of NRG1 with LIM kinase 1 (Wang et al., 1998; Yin et al., 2013a), a major regulator of spine growth (Mizuno, 2013). Whereas we favor this model, ErbB4 expressed in projection neurons and interneurons was shown to regulate spine growth (Cooper and Koleske, 2014;

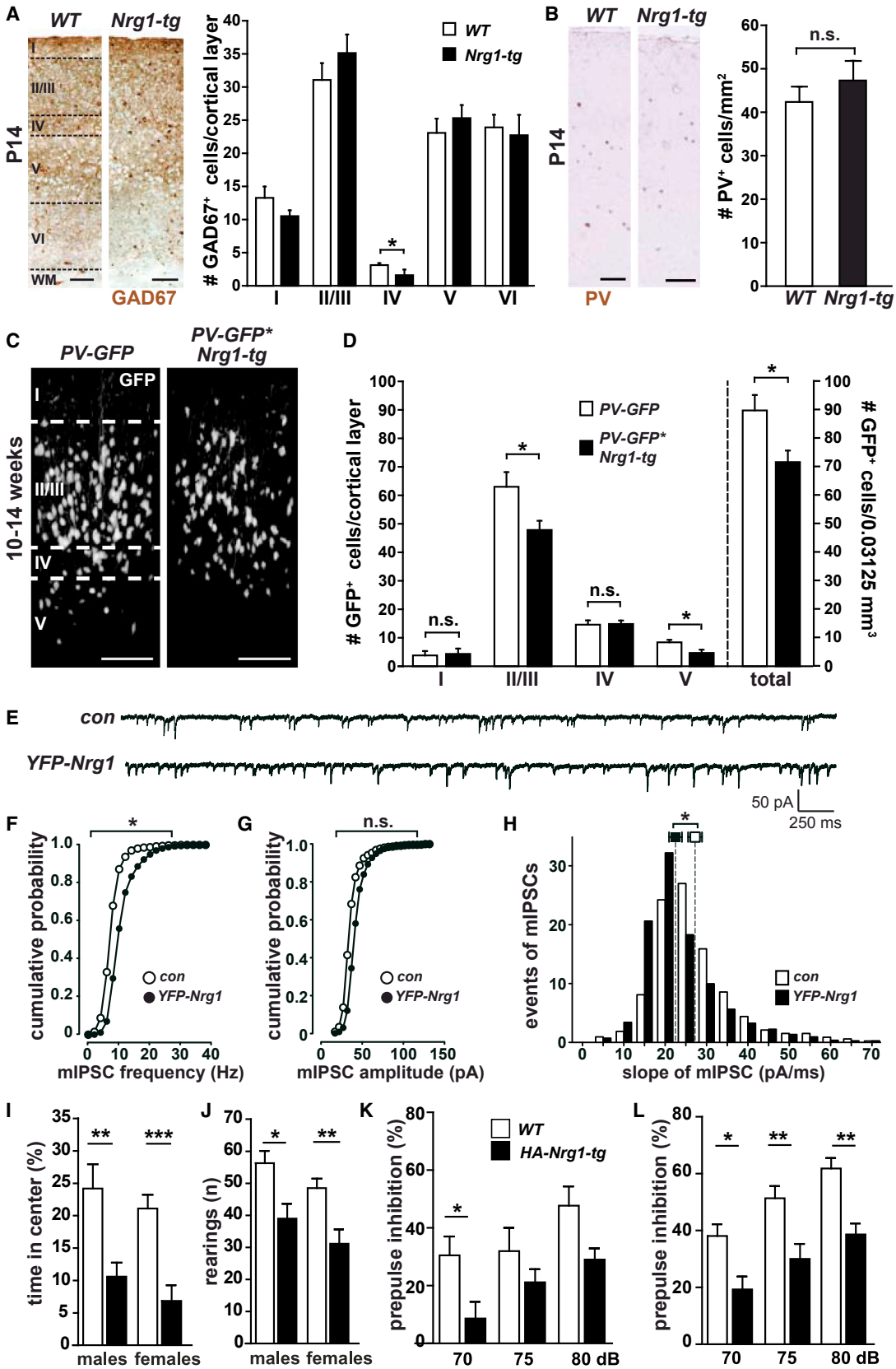

(legend on next page)

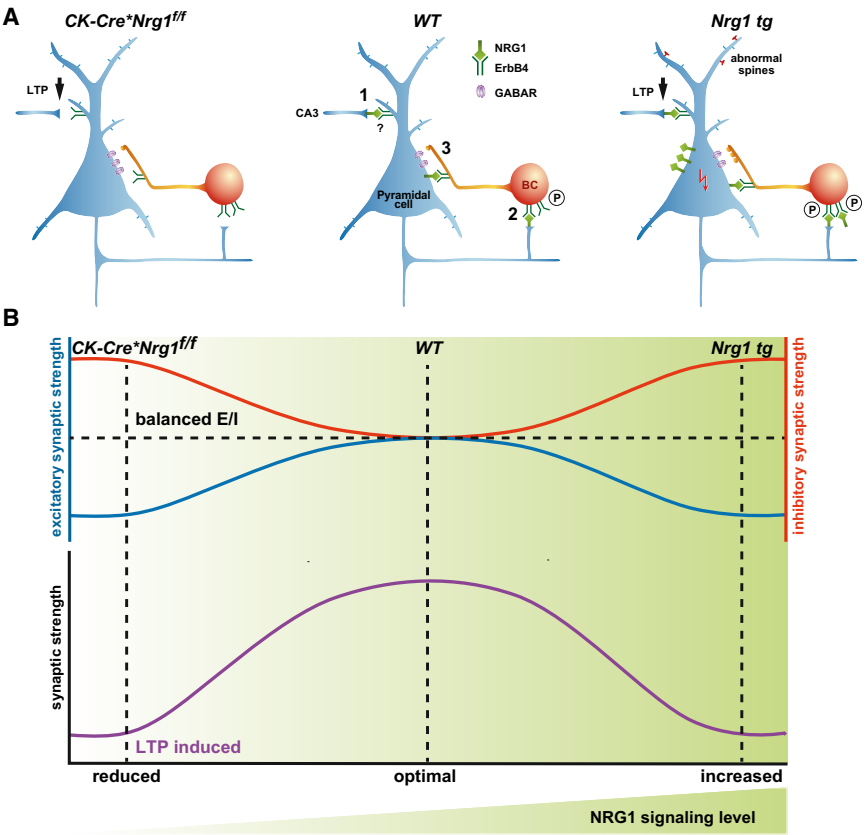

Figure 8. Bell-Shaped Model of NRG1-Mediated Signaling in the Cortex

(A) Middle, sites of possible NRG1/ErbB4 interactions in a simple microcircuit of the hippocampal CA1 region in wild-type. (1) Excitatory CA3/CA1 (Schaffer collateral) synapse. (2) Excitatory pyramidal cell synapse on inhibitory (PV^+) basket cell (BC). (3) Inhibitory BC synapse on pyramidal cell. Question mark indicates uncertain ErbB4 expression in pyramidal cells. Left, absence of pyramidal cell-derived NRG1 signaling (*CK*Nrg1*$^{f/f}$ mutant mice) leads to LTP impairment at the CA1/CA3 synapse and increased IPSC amplitudes, consistent with elevated expression/function of GABA receptors. Right, CRD-NRG1 overexpression in pyramidal cells (*Nrg1-tg* mice) promotes ErbB4 hyperphosphorylation and inhibitory synapse formation/function in BC (as indicated by increased IPSC frequency) and leads to impaired LTP at the CA1/CA3 synapse and abnormal spine growth. LTP and spine defects may result, at least in part, from somatodendritic CRD-NRG1 accumulation and aberrant "back-signaling" (red flash), partly independent from ErbB4.

(B) Both chronically reduced and increased levels of NRG1 signaling cause enhanced inhibitory synaptic strength and reduced excitatory synaptic strength, leading to a dysbalanced E/I ratio and impaired hippocampal LTP.

Del Pino et al., 2013; Yin et al., 2013b). Thus, abnormal spine morphology could directly result from chronic hyperstimulation of ErbB4 receptors. In summary, our data support the hypothesis that abnormal spine growth, observed in schizophrenia patients (Penzes et al., 2011), could be induced by hyperstimulated CRD-NRG1 signaling.

Ventricular enlargement is the most-replicated endophenotype in schizophrenia, and variants of the *NRG1* gene are associated with increased lateral ventricle volume in schizophrenia patients (Mata et al., 2009). We observed reduced ventricular size in *Emx*Nrg1*$^{f/f}$ mutants but enlarged lateral ventricles in *Nrg1-tg* mice. Ventricular size is not affected in Ig-NRG1 transgenic mice (P. Harrison, personal communication). These findings suggest a specific role of CRD-NRG1 in the regulation of ventricular volume. Thus, chronically increased CRD-NRG1 expression could represent a risk factor for ventricular enlargement observed in schizophrenia patients.

In summary, our in vivo data demonstrate that both chronically reduced and increased NRG1 signaling interferes with balanced neurotransmission and synaptic plasticity. Our

Figure 7. Disturbed Inhibitory Circuitry, Anxiety-like Behavior, and Reduced PPI in *Nrg1-tg* Mice

(A) (Left) Immunostaining for GAD67 on coronal brain sections from *WT* and *Nrg1-tg mice* at P14 (somatosensory cortex; bregma −1.7). The scale bars represent 100 μm. (Right) Quantification of $GAD67^+$ interneurons (n = 6/genotype; *p < 0.05, Mann-Whitney U test). I–VI, cortical layers; WM, white matter.

(B) (Left) Immunostaining for PV as in (A). The scale bars represent 100 μm. (Right) Quantification of PV^+ interneurons across all cortical layers (n = 6/genotype; Mann-Whitney U test).

(C) 2P-LSM of *PV-GFP*Nrg1-tg* and *PV-GFP* control mice. Depicted are 3D projections-rendered live-imaging stacks of a cortical column (250 × 250 × 500 μm^3; 2 μm stack interval) from the MZ to layer V.

(D) Quantification of GFP^+ interneurons in layers I–V from 2P-LSM live-imaging stacks. Note that parts of layers V and VI could not be imaged. *PV-GFP*Nrg1-tg*, n = 6; *PV-GFP*, n = 5; *p < 0.05; Student's t test.

(E) Representative recordings of GABAergic mIPSCs from YFP^+ projection neurons in layer V of *Thy1.2-YFP*Nrg1-tg* (*YFP-Nrg1*) and *Thy1.2-YFP* (*con*) mice.

(F and G) Cumulative probabilities of mIPSC frequencies (F) and amplitudes (G) in YFP^+ neurons from *YFP-Nrg1* (n = 17) and control (n = 15) mice.

(H) Onset kinetics expressed as normalized histograms of rise slopes (peak amplitude in pA over time to onset in ms) of GABAergic mIPSCs. Mean values and the significance of onset kinetics are indicated by squares positioned relative to the x axis. *p < 0.05; Mann-Whitney U test.

(I) *HA-Nrg1-tg* mice (age 2 to 3 months) spent less time in the center of the open-field arena when compared with *WT*.

(J) *HA-Nrg1-tg* mice performed less rearings than *WT* in the open-field test.

(K and L) Reduced PPI in male (K) and female (L) *HA-Nrg1-tg* mice. Males: effect of genotype $F_{(1,32)} = 4.31$; *p < 0.05 for prepulse 70 dB; females: effect of genotype $F_{(1,24)} = 16.09$; ***p < 0.001; two-way ANOVA; Bonferroni posttest. (I–L): *WT*: males, n = 18; females, n = 18; *HA-Nrg1-tg* mice: males, n = 16; females, n = 10. Error bars represent SEM.

findings extend an "inverted U" model of NRG1 signaling (Role and Talmage, 2007), and we propose a bell-shaped model, according to which an "optimal" level of NRG1 is required for the establishment, refinement, and "homeostasis" of synaptic neurotransmission. Although chronically reduced NRG1 signaling in the brain impairs synaptic functions, our data suggest that it is chronically increased CRD-NRG1 signaling that phenocopies several endophenotypes described for schizophrenia patients. Thus, CRD-NRG1 transgenic mice could provide a robust preclinical model for further studies of schizophrenia and to facilitate the discovery and development of treatment strategies.

EXPERIMENTAL PROCEDURES

Transgenic and Mutant Mice

The generation and genotyping of conditional *null* mutants of *Nrg1* (Li et al., 2002) and transgenic lines CRD-NRG1 (Michailov et al., 2004), HA-CRD-NRG1 (Velanac et al., 2012), PV-GFP (Meyer et al., 2002), Emx1-Cre (Gorski et al., 2002), and CamKIIα-Cre (Minichiello et al., 1999) has been described. Primer sequences are available upon request. All animal experiments were carried out in compliance with approved animal policies of the Max Planck Institute of Experimental Medicine.

RNA Analysis

Total RNA was extracted using Qiazol Reagent (QIAGEN). cDNA was synthesized from total RNA using random nonamer primers and Superscript III RNase H reverse transcriptase (Invitrogen). Quantitative real-time PCR was carried out using the ABI Prism 7700 Sequence Detection System as described (Brinkmann et al., 2008) and analyzed with 7500 Fast System SDS software version 1.3 (Applied Biosystems) and GraphPad Prism 5.0. PCR primer sequences are available upon request.

Protein Analysis

Brain tissue was homogenized in sucrose or radioimmunoprecipitation assay buffer with protease inhibitors (Complete tablets; Roche). For western blotting, 5–50 μg of protein lysate was size separated on 8% SDS-polyacrylamide gels and blotted onto polyvinylidene fluoride membranes (Hybond-P; Invitrogen) according to manufacturer's instructions. Membranes were incubated with primary antibodies as described in Supplemental Experimental Procedures. The densitometric analysis of scanned enhanced chemiluminescence films was carried out using ImageJ and GraphPad Prism 5.0. Data are displayed as SEM, and statistical significance was tested using a Mann-Whitney U test.

Synaptosomes and Synaptic Plasma Membrane Preparation

Synaptosomes were isolated by a sucrose density gradient technique (Dodd et al., 1981) modified to isolate synaptosomes from small quantities of starting material (detailed in Supplemental Experimental Procedures). Synaptosomes were fractionated into Triton X-100 soluble (synaptic membranes) and insoluble (mainly postsynaptic density proteins) fractions by ultracentrifugation (Mizoguchi et al., 1989). The Triton X-100 insoluble fraction was solubilized using 2% SDS buffer. Analysis was performed using SDS-PAGE and western blotting as described above and in Supplemental Experimental Procedures.

Proteomics

Proteins were extracted from hippocampal tissue, followed by separation on SDS-polyacrylamide gels and enzymatic digestion with trypsin. Resulting peptides were analyzed on a Waters quadrupole time-of-flight Premier mass spectrometer as described (Martins-de-Souza et al., 2007). Wilcoxon signed-rank tests were used to determine statistical significance ($p < 0.05$).

Histology and Immunostaining

Free-floating vibratome (40–50 μm) or paraffin sections (5 μm) were incubated overnight with primary antibodies as described in Supplemental Experimental Procedures. Sections were incubated with secondary antibodies Cy2 (1:10,000; Jackson ImmunoResearch), Cy3 (1:10,000; Jackson ImmunoResearch), Alexa 488 and Alexa Fluor 555 (1:2,000; Invitrogen) for 1 hr at room temperature. For the analysis of neurodegenerative changes, paraplast-embedded sections (5–7 μm) were stained with hematoxylin and eosin staining (Merck) and Cresyl Violet. Digital images were obtained using 510-meta LSM and Axiophot (Zeiss) and DMRXA (Leica) microscopes. All images were processed with ImageJ.

Electrophysiology

Transverse slices (300 μm) were cut from mouse brain (10–12 weeks old) and transferred to a recording chamber filled with artificial cerebrospinal fluid. Field recording data were digitized by DigiData 1322A and analyzed using Clampfit 10.0 (Molecular Devices). During whole-cell patch recordings, sIPSCs were recorded at a holding potential of -70 mV in the presence of 10 μM 6-cyano-7-nitroquinoxaline-2,3-dione and 40 μM 2-amino-5-phosphonopentanoic acid; sEPSCs were recorded in the presence of 5 μM strychnine and 5 μM bicuculline. For mIPSC and mEPSC recording, 0.5 μM tetrodotoxin was added to the bath solution. Data acquisition and analysis was carried out using pClamp 10.0 (Molecular Devices), MiniAnalysis (SynaptoSoft), and Prism 4 (GraphPad). Statistical significance was evaluated using a two-tailed unpaired Student's t test with Welch's correction or a Mann-Whitney U test. Significance level was set to $p < 0.05$, and values are displayed as SEM. For details, see the Supplemental Experimental Procedures.

MRI and Volumetry

Mice were anesthetized with 5% isofluorane, intubated, and kept under anesthesia with 1%–1.5% isofluorane in oxygen and ambient air (1:1.5). MRI was performed at a field strength of 2.35 T (Bruker Biospin MRI) using a T1-weighted 3D FLASH sequence as described (Natt et al., 2002), reaching an isotropic resolution of 117 μm. Total brain volume (excluding olfactory bulb, cerebellum, and brainstem) and, separately, the size of the lateral and third ventricles, cerebellum, olfactory bulb, and brainstem were determined by manually drawing respective regions of interest on up to 50 contiguous horizontal MRI sections.

In Vivo 2P-LSM and In Vivo STED Nanoscopy

Two-photon microscopy (Agarwal et al., 2012) and STED imaging (Berning et al., 2012) were performed as described. See the Supplemental Experimental Procedures for details.

Behavioral Testing

For behavioral experiments, age-matched *CK-Cre*Nrg1*$^{f/f}$, *CK-Cre*Nrg1*$^{f/+}$, *Nrg1*$^{f/+}$, *HA-Nrg1-tg*, and WT mice at 12–15 weeks of age were used. Three to five mice per cage were housed in a room with a 12 hr light-dark cycle (lights on at 9:00 a.m.) with ad libitum access to food and water. Behavioral tests were conducted in a blinded fashion during the light phase (10:00 a.m.–5:00 p.m.) as described in Brzózka et al. (2010). Data are displayed as SEM, and statistical significance was analyzed using a Mann-Whitney U test and a two-way ANOVA with Bonferroni posttest (for multiple group comparisons). See the Supplemental Experimental Procedures for details. All experiments were performed with permission from the local Animal Care and Use Committee (Bezirksregierung Braunschweig) in accordance with the German Animal Protection Law.

SUPPLEMENTAL INFORMATION

Supplemental Information includes Supplemental Experimental Procedures, seven figures, and four tables and can be found with this article online at http://dx.doi.org/10.1016/j.celrep.2014.07.026.

AUTHOR CONTRIBUTIONS

A.A. generated *CamKII-Cre*Nrg1* and *Emx1-Cre*Ngr1* mice and carried out biochemical, histological and gene expression analysis on NRG1 conditional mutants and transgenic mice. M.Z., I.T.-D., Z.T., and W.Z. performed electrophysiological analysis. T.U. contributed to histological, biochemical, and behavioral analysis of *Emx1-Cre*Nrg1* mutants and transgenic mice. K.R.,

T.U., M.M.B., M.J.R., and H.E. carried out behavioral analysis. M.N.G. generated *HA-Nrg1* transgenic mice. A.A., S. Boretius, and J.F. performed MRI-based volumetric analysis. P.D. performed in vivo 2P-LSM. S. Berning, H.S., K.I.W., and S.W.H. were responsible for STED imaging. D.M.d.S., P.C.G., and S. Bahn carried out proteomic analysis. K.-A.N. and H.E. contributed conceptual ideas and supervised experiments. A.A., W.Z., and M.H.S. designed the study, analyzed data, and wrote the manuscript. All authors read and approved the final manuscript.

ACKNOWLEDGMENTS

We thank A. Fahrenholz and M. Floerl for excellent technical assistance. We also thank C. Casper and D. Flemming for help with animal husbandry. We thank C. Birchmeier for providing conditional NRG1 mutant mice, R. Klein for CamKII-Cre mice, K. Jones for EmxI-Cre mice, F. Kirchhoff for Thy1.2-YFP mice, and H. Monyer for PV-GFP mice. We thank N. Brose, S. Papiol, S. Wichert, and members of the Department of Neurogenetics for helpful discussions. A.A. is supported by a Postdoctoral Fellowship from the National Multiple Sclerosis Society. W.Z. is supported by the IZKF of the University of Münster Medical School (Zha3-005-14). M.J.R. and M.M.B. were supported by the Deutsche Forschungsgemeinschaft (Klinische Forschergruppe [KFO] 241: RO 4076/1-1). S.W.H., W.Z., M.H.S., and K.-A.N. acknowledge grant support from the Deutsche Forschungsgemeinschaft (DFG Research Center Molecular Physiology of the Brain [CMPB] and SFB TRR58 to W.Z.). M.H.S. is supported by a Heisenberg fellowship from the Deutsche Forschungsgemeinschaft. K.-A.N. holds an ERC Advanced Grant.

Received: November 25, 2013
Revised: April 4, 2014
Accepted: July 16, 2014
Published: August 14, 2014

REFERENCES

Agarwal, A., Dibaj, P., Kassmann, C.M., Goebbels, S., Nave, K.A., and Schwab, M.H. (2012). In vivo imaging and noninvasive ablation of pyramidal neurons in adult NEX-CreERT2 mice. Cereb. Cortex *22*, 1473–1486.

Ayalew, M., Le-Niculescu, H., Levey, D.F., Jain, N., Changala, B., Patel, S.D., Winiger, E., Breier, A., Shekhar, A., Amdur, R., et al. (2012). Convergent functional genomics of schizophrenia: from comprehensive understanding to genetic risk prediction. Mol. Psychiatry *17*, 887–905.

Berning, S., Willig, K.I., Steffens, H., Dibaj, P., and Hell, S.W. (2012). Nanoscopy in a living mouse brain. Science *335*, 551.

Bertram, I., Bernstein, H.G., Lendeckel, U., Bukowska, A., Dobrowolny, H., Keilhoff, G., Kanakis, D., Mawrin, C., Bielau, H., Falkai, P., and Bogerts, B. (2007). Immunohistochemical evidence for impaired neuregulin-1 signaling in the prefrontal cortex in schizophrenia and in unipolar depression. Ann. N Y Acad. Sci. *1096*, 147–156.

Brinkmann, B.G., Agarwal, A., Sereda, M.W., Garratt, A.N., Müller, T., Wende, H., Stassart, R.M., Nawaz, S., Humml, C., Velanac, V., et al. (2008). Neuregulin-1/ErbB signaling serves distinct functions in myelination of the peripheral and central nervous system. Neuron *59*, 581–595.

Brzózka, M.M., Radyushkin, K., Wichert, S.P., Ehrenreich, H., and Rossner, M.J. (2010). Cognitive and sensorimotor gating impairments in transgenic mice overexpressing the schizophrenia susceptibility gene Tcf4 in the brain. Biol. Psychiatry *68*, 33–40.

Cahill, M.E., Remmers, C., Jones, K.A., Xie, Z., Sweet, R.A., and Penzes, P. (2013). Neuregulin1 signaling promotes dendritic spine growth through kalirin. J. Neurochem. *126*, 625–635.

Carraway, K.L., 3rd, Weber, J.L., Unger, M.J., Ledesma, J., Yu, N., Gassmann, M., and Lai, C. (1997). Neuregulin-2, a new ligand of ErbB3/ErbB4-receptor tyrosine kinases. Nature *387*, 512–516.

Chen, Y.J., Johnson, M.A., Lieberman, M.D., Goodchild, R.E., Schobel, S., Lewandowski, N., Rosoklija, G., Liu, R.C., Gingrich, J.A., Small, S., et al. (2008). Type III neuregulin-1 is required for normal sensorimotor gating, memory-related behaviors, and corticostriatal circuit components. J. Neurosci. *28*, 6872–6883.

Chen, Y.J., Zhang, M., Yin, D.M., Wen, L., Ting, A., Wang, P., Lu, Y.S., Zhu, X.H., Li, S.J., Wu, C.Y., et al. (2010). ErbB4 in parvalbumin-positive interneurons is critical for neuregulin 1 regulation of long-term potentiation. Proc. Natl. Acad. Sci. USA *107*, 21818–21823.

Cooper, M.A., and Koleske, A.J. (2014). Ablation of ErbB4 from excitatory neurons leads to reduced dendritic spine density in mouse prefrontal cortex. J. Comp. Neurol. *522*, 3351–3362.

Deakin, I.H., Nissen, W., Law, A.J., Lane, T., Kanso, R., Schwab, M.H., Nave, K.A., Lamsa, K.P., Paulsen, O., Bannerman, D.M., and Harrison, P.J. (2012). Transgenic overexpression of the type I isoform of neuregulin 1 affects working memory and hippocampal oscillations but not long-term potentiation. Cereb. Cortex *22*, 1520–1529.

Del Pino, I., García-Frigola, C., Dehorter, N., Brotons-Mas, J.R., Alvarez-Salvado, E., Martínez de Lagrán, M., Ciceri, G., Gabaldón, M.V., Moratal, D., Dierssen, M., et al. (2013). Erbb4 deletion from fast-spiking interneurons causes schizophrenia-like phenotypes. Neuron *79*, 1152–1168.

Deutsch, S.I., Rosse, R.B., and Mastropaolo, J. (1997). Behavioral approaches to the functional assessment of NMDA-mediated neural transmission in intact mice. Clin. Neuropharmacol. *20*, 375–384.

Dodd, P.R., Hardy, J.A., Oakley, A.E., Edwardson, J.A., Perry, E.K., and Delaunoy, J.P. (1981). A rapid method for preparing synaptosomes: comparison, with alternative procedures. Brain Res. *226*, 107–118.

Falls, D.L. (2003). Neuregulins: functions, forms, and signaling strategies. Exp. Cell Res. *284*, 14–30.

Fazzari, P., Paternain, A.V., Valiente, M., Pla, R., Luján, R., Lloyd, K., Lerma, J., Marín, O., and Rico, B. (2010). Control of cortical GABA circuitry development by Nrg1 and ErbB4 signalling. Nature *464*, 1376–1380.

Flames, N., Long, J.E., Garratt, A.N., Fischer, T.M., Gassmann, M., Birchmeier, C., Lai, C., Rubenstein, J.L., and Marín, O. (2004). Short- and long-range attraction of cortical GABAergic interneurons by neuregulin-1. Neuron *44*, 251–261.

Gorski, J.A., Talley, T., Qiu, M., Puelles, L., Rubenstein, J.L., and Jones, K.R. (2002). Cortical excitatory neurons and glia, but not GABAergic neurons, are produced in the Emx1-expressing lineage. J. Neurosci. *22*, 6309–6314.

Gu, Z., Jiang, Q., Fu, A.K., Ip, N.Y., and Yan, Z. (2005). Regulation of NMDA receptors by neuregulin signaling in prefrontal cortex. J. Neurosci. *25*, 4974–4984.

Hahn, C.G., Wang, H.Y., Cho, D.S., Talbot, K., Gur, R.E., Berrettini, W.H., Bakshi, K., Kamins, J., Borgmann-Winter, K.E., Siegel, S.J., et al. (2006). Altered neuregulin 1-erbB4 signaling contributes to NMDA receptor hypofunction in schizophrenia. Nat. Med. *12*, 824–828.

Hering, H., and Sheng, M. (2001). Dendritic spines: structure, dynamics and regulation. Nat. Rev. Neurosci. *2*, 880–888.

Hirrlinger, P.G., Scheller, A., Braun, C., Quintela-Schneider, M., Fuss, B., Hirrlinger, J., and Kirchhoff, F. (2005). Expression of reef coral fluorescent proteins in the central nervous system of transgenic mice. Mol. Cell. Neurosci. *30*, 291–303.

Huang, Y.Z., Won, S., Ali, D.W., Wang, Q., Tanowitz, M., Du, Q.S., Pelkey, K.A., Yang, D.J., Xiong, W.C., Salter, M.W., and Mei, L. (2000). Regulation of neuregulin signaling by PSD-95 interacting with ErbB4 at CNS synapses. Neuron *26*, 443–455.

Jiang, L., Emmetsberger, J., Talmage, D.A., and Role, L.W. (2013). Type III neuregulin 1 is required for multiple forms of excitatory synaptic plasticity of mouse cortico-amygdala circuits. J. Neurosci. *33*, 9655–9666.

Kwon, O.B., Longart, M., Vullhorst, D., Hoffman, D.A., and Buonanno, A. (2005). Neuregulin-1 reverses long-term potentiation at CA1 hippocampal synapses. J. Neurosci. *25*, 9378–9383.

Law, A.J., Lipska, B.K., Weickert, C.S., Hyde, T.M., Straub, R.E., Hashimoto, R., Harrison, P.J., Kleinman, J.E., and Weinberger, D.R. (2006). Neuregulin 1 transcripts are differentially expressed in schizophrenia and regulated by 5′ SNPs associated with the disease. Proc. Natl. Acad. Sci. USA *103*, 6747–6752.

Li, L., Cleary, S., Mandarano, M.A., Long, W., Birchmeier, C., and Jones, F.E. (2002). The breast proto-oncogene, HRGalpha regulates epithelial proliferation and lobuloalveolar development in the mouse mammary gland. Oncogene *21*, 4900–4907.

Li, D., Collier, D.A., and He, L. (2006). Meta-analysis shows strong positive association of the neuregulin 1 (NRG1) gene with schizophrenia. Hum. Mol. Genet. *15*, 1995–2002.

Li, K.X., Lu, Y.M., Xu, Z.H., Zhang, J., Zhu, J.M., Zhang, J.M., Cao, S.X., Chen, X.J., Chen, Z., Luo, J.H., et al. (2012). Neuregulin 1 regulates excitability of fast-spiking neurons through Kv1.1 and acts in epilepsy. Nat. Neurosci. *15*, 267–273.

Liu, X., Bates, R., Yin, D.M., Shen, C., Wang, F., Su, N., Kirov, S.A., Luo, Y., Wang, J.Z., Xiong, W.C., and Mei, L. (2011). Specific regulation of NRG1 isoform expression by neuronal activity. J. Neurosci. *31*, 8491–8501.

Martins-de-Souza, D., Menezes de Oliveira, B., dos Santos Farias, A., Horiuchi, R.S., Crepaldi Domingues, C., de Paula, E., Marangoni, S., Gattaz, W.F., Dias-Neto, E., and Camillo Novello, J. (2007). The use of ASB-14 in combination with CHAPS is the best for solubilization of human brain proteins for two-dimensional gel electrophoresis. Brief. Funct. Genomic Proteomic *6*, 70–75.

Mata, I., Perez-Iglesias, R., Roiz-Santiañez, R., Tordesillas-Gutierrez, D., Gonzalez-Mandly, A., Vazquez-Barquero, J.L., and Crespo-Facorro, B. (2009). A neuregulin 1 variant is associated with increased lateral ventricle volume in patients with first-episode schizophrenia. Biol. Psychiatry *65*, 535–540.

Meyer, D., and Birchmeier, C. (1995). Multiple essential functions of neuregulin in development. Nature *378*, 386–390.

Meyer, A.H., Katona, I., Blatow, M., Rozov, A., and Monyer, H. (2002). In vivo labeling of parvalbumin-positive interneurons and analysis of electrical coupling in identified neurons. J. Neurosci. *22*, 7055–7064.

Michailov, G.V., Sereda, M.W., Brinkmann, B.G., Fischer, T.M., Haug, B., Birchmeier, C., Role, L., Lai, C., Schwab, M.H., and Nave, K.A. (2004). Axonal neuregulin-1 regulates myelin sheath thickness. Science *304*, 700–703.

Miles, R., Tóth, K., Gulyás, A.I., Hájos, N., and Freund, T.F. (1996). Differences between somatic and dendritic inhibition in the hippocampus. Neuron *16*, 815–823.

Minichiello, L., Korte, M., Wolfer, D., Kühn, R., Unsicker, K., Cestari, V., Rossi-Arnaud, C., Lipp, H.P., Bonhoeffer, T., and Klein, R. (1999). Essential role for TrkB receptors in hippocampus-mediated learning. Neuron *24*, 401–414.

Mizoguchi, A., Ueda, T., Ikeda, K., Shiku, H., Mizoguti, H., and Takai, Y. (1989). Localization and subcellular distribution of cellular ras gene products in rat brain. Brain Res. Mol. Brain Res. *5*, 31–44.

Mizuno, K. (2013). Signaling mechanisms and functional roles of cofilin phosphorylation and dephosphorylation. Cell. Signal. *25*, 457–469.

Natt, O., Watanabe, T., Boretius, S., Radulovic, J., Frahm, J., and Michaelis, T. (2002). High-resolution 3D MRI of mouse brain reveals small cerebral structures in vivo. J. Neurosci. Methods *120*, 203–209.

Nave, K.A., and Salzer, J.L. (2006). Axonal regulation of myelination by neuregulin 1. Curr. Opin. Neurobiol. *16*, 492–500.

Neddens, J., and Buonanno, A. (2010). Selective populations of hippocampal interneurons express ErbB4 and their number and distribution is altered in ErbB4 knockout mice. Hippocampus *20*, 724–744.

Ozaki, M., Sasner, M., Yano, R., Lu, H.S., and Buonanno, A. (1997). Neuregulin-beta induces expression of an NMDA-receptor subunit. Nature *390*, 691–694.

Penzes, P., Cahill, M.E., Jones, K.A., VanLeeuwen, J.E., and Woolfrey, K.M. (2011). Dendritic spine pathology in neuropsychiatric disorders. Nat. Neurosci. *14*, 285–293.

Pitcher, G.M., Beggs, S., Woo, R.S., Mei, L., and Salter, M.W. (2008). ErbB4 is a suppressor of long-term potentiation in the adult hippocampus. Neuroreport *19*, 139–143.

Pitcher, G.M., Kalia, L.V., Ng, D., Goodfellow, N.M., Yee, K.T., Lambe, E.K., and Salter, M.W. (2011). Schizophrenia susceptibility pathway neuregulin 1-ErbB4 suppresses Src upregulation of NMDA receptors. Nat. Med. *17*, 470–478.

Role, L.W., and Talmage, D.A. (2007). Neurobiology: new order for thought disorders. Nature *448*, 263–265.

Shamir, A., Kwon, O.B., Karavanova, I., Vullhorst, D., Leiva-Salcedo, E., Janssen, M.J., and Buonanno, A. (2012). The importance of the NRG-1/ErbB4 pathway for synaptic plasticity and behaviors associated with psychiatric disorders. J. Neurosci. *32*, 2988–2997.

Stefansson, H., Sigurdsson, E., Steinthorsdottir, V., Bjornsdottir, S., Sigmundsson, T., Ghosh, S., Brynjolfsson, J., Gunnarsdottir, S., Ivarsson, O., Chou, T.T., et al. (2002). Neuregulin 1 and susceptibility to schizophrenia. Am. J. Hum. Genet. *71*, 877–892.

Tan, G.H., Liu, Y.Y., Hu, X.L., Yin, D.M., Mei, L., and Xiong, Z.Q. (2012). Neuregulin 1 represses limbic epileptogenesis through ErbB4 in parvalbumin-expressing interneurons. Nat. Neurosci. *15*, 258–266.

Ting, A.K., Chen, Y., Wen, L., Yin, D.M., Shen, C., Tao, Y., Liu, X., Xiong, W.C., and Mei, L. (2011). Neuregulin 1 promotes excitatory synapse development and function in GABAergic interneurons. J. Neurosci. *31*, 15–25.

Trommald, M., Hulleberg, G., and Andersen, P. (1996). Long-term potentiation is associated with new excitatory spine synapses on rat dentate granule cells. Learn. Mem. *3*, 218–228.

Uhlhaas, P.J., and Singer, W. (2010). Abnormal neural oscillations and synchrony in schizophrenia. Nat. Rev. Neurosci. *11*, 100–113.

Velanac, V., Unterbarnscheidt, T., Hinrichs, W., Gummert, M.N., Fischer, T.M., Rossner, M.J., Trimarco, A., Brivio, V., Taveggia, C., Willem, M., et al. (2012). Bace1 processing of NRG1 type III produces a myelin-inducing signal but is not essential for the stimulation of myelination. Glia *60*, 203–217.

Wang, J.Y., Frenzel, K.E., Wen, D., and Falls, D.L. (1998). Transmembrane neuregulins interact with LIM kinase 1, a cytoplasmic protein kinase implicated in development of visuospatial cognition. J. Biol. Chem. *273*, 20525–20534.

Weickert, C.S., Tiwari, Y., Schofield, P.R., Mowry, B.J., and Fullerton, J.M. (2012). Schizophrenia-associated HapICE haplotype is associated with increased NRG1 type III expression and high nucleotide diversity. Transl. Psychiatr. *2*, e104.

Wen, L., Lu, Y.S., Zhu, X.H., Li, X.M., Woo, R.S., Chen, Y.J., Yin, D.M., Lai, C., Terry, A.V., Jr., Vazdarjanova, A., et al. (2010). Neuregulin 1 regulates pyramidal neuron activity via ErbB4 in parvalbumin-positive interneurons. Proc. Natl. Acad. Sci. USA *107*, 1211–1216.

Woo, R.S., Li, X.M., Tao, Y., Carpenter-Hyland, E., Huang, Y.Z., Weber, J., Neiswender, H., Dong, X.P., Wu, J., Gassmann, M., et al. (2007). Neuregulin-1 enhances depolarization-induced GABA release. Neuron *54*, 599–610.

Yin, D.M., Chen, Y.J., Lu, Y.S., Bean, J.C., Sathyamurthy, A., Shen, C., Liu, X., Lin, T.W., Smith, C.A., Xiong, W.C., and Mei, L. (2013a). Reversal of behavioral deficits and synaptic dysfunction in mice overexpressing neuregulin 1. Neuron *78*, 644–657.

Yin, D.M., Sun, X.D., Bean, J.C., Lin, T.W., Sathyamurthy, A., Xiong, W.C., Gao, T.M., Chen, Y.J., and Mei, L. (2013b). Regulation of spine formation by ErbB4 in PV-positive interneurons. J. Neurosci. *33*, 19295–19303.

Zhong, C., Du, C., Hancock, M., Mertz, M., Talmage, D.A., and Role, L.W. (2008). Presynaptic type III neuregulin 1 is required for sustained enhancement of hippocampal transmission by nicotine and for axonal targeting of alpha7 nicotinic acetylcholine receptors. J. Neurosci. *28*, 9111–9116.